Stirring and transport enhancement in a continuously modulated free-surface flow

By MARK C. T. WILSON, J. L. SUMMERS,
N. KAPUR AND P. H. GASKELL

School of Mechanical Engineering, University of Leeds, LS2 9JT, UK

The transport of fluid from a recirculation region adjacent to a free surface is studied using a numerical method validated with experimental flow visualization. The flow is an example of a liquid film coating process, and consists of two counter-rotating rolls placed side-by-side and half-submerged in a bath of fluid. In the gap between the rolls a recirculation zone exists just below the free surface, around which the flow splits into two films. Fluid recirculating for long periods has been identified as a source of coating defects, so this paper considers a possible method of inducing stirring. The flow is modulated by driving one of the rolls through a Hooke's joint, which delivers a well-characterized periodic perturbation to the roll speed. In response to this speed modulation, the free surface undergoes a periodic change in position and shape which drives an exchange of fluid between the recirculation region and the surrounding flow. The amplitude of the free-surface motion is strongly dependent on modulation frequency.

The dynamics of the free surface preclude a quasi-steady approach, even in the small-frequency limit, and so a fully time-dependent analysis based on the finite element method is employed. Trigonometric temporal interpolation of the finite element data is used to make passive tracer advection calculations more efficient, and excellent agreement is seen between simulation and experiment. Computations of the stable and unstable invariant manifolds associated with periodic points on the free surface reveal that the exchange of fluid is governed by a self-intersecting turnstile mechanism, by which most fluid entrained during a modulation cycle is ejected later in the same cycle.

Transport over several cycles is explored by observation of the evacuation of passive tracers initially distributed uniformly in the recirculation zone. Results demonstrate the persistence of unmixed cores whose size is dependent on the modulation frequency. By considering the percentage of tracers remaining after a fixed number of cycles, contours in frequency–amplitude space show that for each modulation amplitude there is a frequency which produces the most effective transport, with up to 80 % of tracers removed by a modulation which produces only a 5 % change in film thickness. Finally it is shown how modulation of both rolls at slightly different phases can reduce the film thickness variation to about 1 % while maintaining the level of transport.

1. Introduction

Two-dimensional steady laminar fluid flows in bounded domains often feature regions of recirculation in which fluid is trapped and separated from the rest of the flow. Under steady conditions eddies persist since fluid may not cross their bounding

streamlines; passive 'tracer' particles placed within a recirculation would execute non-chaotic closed orbits (Aref 1984). However, there are several ways in which such steady flows can be modulated in time to produce chaotic fluid motion and an interaction between fluid within a recirculation and that outside it. Indeed, following Aref's (1984) seminal work on 'stirring by chaotic advection' an extensive body of literature dedicated to the theoretical, computational and experimental study of this phenomenon has been accumulated. For a discussion of earlier work on mixing, see for example Ottino (1989).

Two of the most popular geometries studied are the journal bearing (e.g. Swanson & Ottino 1990; Kaper & Wiggins 1993; Kumar & Homsy 1996; Galaktionov, Anderson & Peters 2002) and the rectangular double-lid-driven cavity (e.g. Chien, Rising & Ottino 1986; Anderson *et al.* 2000*a*). In both of these systems the flow is driven by the tangential motion of two boundaries, i.e. the rotation of the inner and outer cylinders or the parallel translational motion of the two lids, and chaotic flow can be achieved by varying the speeds of these boundaries periodically in so-called modulation 'protocols'. Protocols can be discontinuous, involving the alternating steady motion of one boundary then the other (e.g. Swanson & Ottino 1990), or continuous, for example the sinusoidal modulations of Kaper & Wiggins (1993). In both cases the geometry of the domain does not vary with time.

An alternative means of generating chaos is to modulate the shape of the domain through non-tangential motion of one or more boundaries. This was first done in the 'baffled cavity flow' by Jana, Tjahjadi & Ottino (1994). The flow consisted of a rectangular driven cavity into which a number of baffles were periodically inserted and withdrawn. The presence of the baffles was found to improve mixing greatly, and led to innovations in the design of screw extruders (Tjahjadi & Foster 1996; Yao *et al.* 1997). More recently, Finn & Cox (2001) studied the stirring effect of a circular cylindrical rod moving on a cycloidal path through a static cylindrical container of fluid. Under the assumption of two-dimensional Stokes flow, they used a complex-variable formulation to obtain an analytical representation of the flow field. Again, this geometric modulation of the domain was found to give good mixing.

A further example, of particular relevance to the present work, is provided by Horner *et al.* (2002), who studied the flow in a rectangular cavity with three solid sides and one side open to an annular channel; the perturbation to the steady flow was caused by the rotating inner cylinder. Two types of periodic flow modulation were explored: a purely temporal one produced by variation of the speed of the circular inner cylinder, and a spatial one effected by introducing ribs onto the surface of the cylinder which was then rotated at constant rate. The exchange of fluid between the cavity and the channel was described in terms of the dynamics of lobes bounded by intersecting segments of invariant manifolds associated with the separation points in the cavity. These ideas are also applied in the present study, and hence the work of Horner *et al.* (2002) will be referred to again in later sections. Recently Wierschem & Aksel (2004) have observed experimentally fluid transport from an eddy in the trough of a sinusoidal substrate over which a liquid flows. The flow is very similar to that of Horner *et al.* (2002) except that the time-dependence of the flow comes from waves on the surface of the film.

The problem of interest here features aspects of both the fixed-domain modulated-speed flows and the geometrically modulated flows, since it involves a flow between two (solid) rotating cylinders and includes a free surface whose position and shape change in response to the speeds of the cylinders. The flow arises in the coating industry, where it is sometimes known as 'inlet-flooded forward roll coating', and it
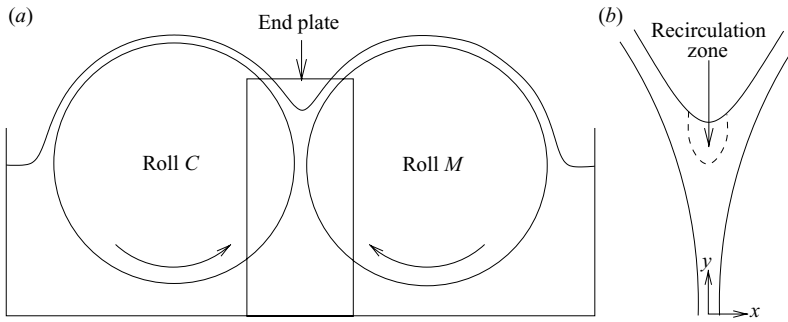
FIGURE 1. Schematic showing a cross-section of the experimental rig (*a*), and the computational domain (*b*). Roll *C* rotates at constant speed, while the speed of roll *M* is modulated.

has been analysed both in the steady state (e.g. Coyle, Macosko & Scriven 1986; Gaskell, Savage & Thompson 1998*b*) and to predict the onset of interfacial instability (e.g. Coyle, Macosko & Scriven 1990). Figure 1 shows the experimental realization of the flow and the associated computational domain. The rolls are half-submerged in a bath of liquid and counter-rotate to produce a narrow 'bead' of liquid in the small gap between them. A thin film is drawn out of the bead by each roll, and under normal operating conditions a substrate would be wound around one of the rolls so that it is continuously coated. Generally, a recirculation zone is present in the 'film-split' region, as indicated in figure 1. Regions of recirculation are undesirable in coating flows (Gaskell *et al.* 1999; Gutoff 1993), however, since fluid trapped inside them can degrade and form solid deposits whose later ejection is detrimental to the quality of the finished coating. In some cases it may be possible to redesign the geometry of the coater to reduce the occurrence of such features (Noakes *et al.* 2002), but where this is not possible it is of interest to investigate possibilities for inducing fluid exchange between the recirculation region and the surrounding flow. The method of flow modulation is one potential means of achieving this.

From a fundamental point of view, a particularly intriguing aspect of this flow is that the free surface – whose response to the modulation is unknown beforehand – forms part of the boundary of one of the eddies in the recirculation zone. The implications of this are discussed in §2, after which §3 describes the experiments and §4 the numerical method. The main results are given in §5, with issues relating to the industrial context of the flow discussed further in §6. The paper is concluded in §7.

2. Flow features and invariant manifolds

The flow structure in steady-state inlet-flooded forward roll coating has been previously studied by, for example, Wicks *et al.* (1995) and Gaskell *et al.* (1998*b*). Figure 2 presents streamlines calculated using a steady-state version of the finite element method described in §4.2. For the flow parameters used here, the flow always features three hyperbolic separation/attachment points, *A*, *B*, *C*, on the free surface, along with a single interior hyperbolic point, *D*, and two elliptic stagnation points (shown as black circles in the figure).

When the roll speeds are equal ($S = 1$), the flow is found to be symmetrical and the interior saddle point is connected to each of the free-surface saddle points, producing two joint eddies attached to the free surface. In the general case, however, the eddies are disjoint: one is attached to the meniscus while the other lies entirely within the
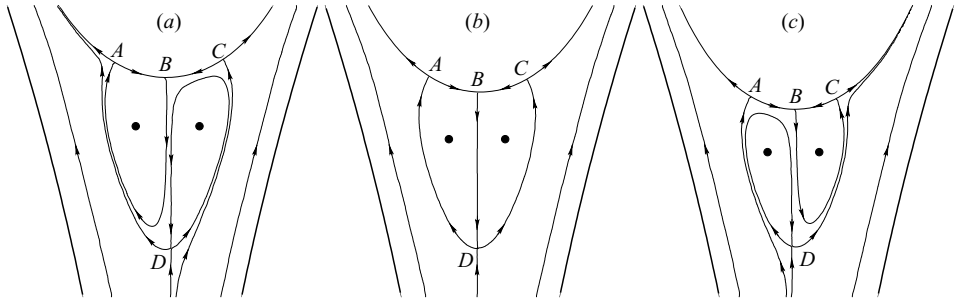
FIGURE 2. Streamlines calculated using a steady-state version of the finite element method described in §4.2. The flow parameters are given in table 1, with the speed ratio given by (*a*) $S = 0.8$, (*b*) $S = 1$, and (*c*) $S = 1.2$. Following the convention of figure 1, S is the ratio of the right-hand roll's speed to that of the left-hand roll. The black circles indicate the rough position of elliptic stagnation points.

domain and is bounded by a homoclinic streamline passing through the interior saddle point. In this asymmetric situation a small amount of fluid from upstream winds its way between the eddies and exits on the faster moving roll. In the roll coating literature, this fluid path is referred to as a 'transfer jet' (Gaskell *et al.* 1995; Summers, Thompson & Gaskell 2004).

When the speed of roll M (the right-hand roll in figure 2) is modulated, the free surface moves alternately towards and away from the 'nip' (the point of minimum separation between the roll surfaces), and the area (i.e. volume per unit axial length) of the recirculation zone changes correspondingly. It is evident therefore that the free surface motion drives an exchange of fluid between the recirculation region and the surrounding flow. The question of interest here is: is the fluid exchange limited to that required by the volumetric change, or are there modulations for which a greater degree of fluid transport can be induced?

In analyses of fluid transport, perhaps the most important conceptual tool is the idea of stable and unstable 'invariant manifolds' in the flow. The behaviour of such manifolds and the role they play in the fluid transport mechanisms for periodic, quasi-periodic and aperiodic flows have been analysed and described in detail in a number of works, e.g. Rom-Kedar & Wiggins (1990), Rom-Kedar, Leonard & Wiggins (1990), Wiggins (1992), Beigie, Leonard & Wiggins (1994), Malhotra & Wiggins (1998), and Horner *et al.* (2002). A brief explanation is given here in the context of the present free-surface flow, to aid the understanding of the results presented later.

In snapshots of a flow, invariant manifolds appear as smooth curves having the property that each point on such a curve remains on that curve, as it evolves, for all time. Therefore fluid cannot cross an invariant manifold except by molecular diffusion, which is regarded as negligible throughout this work. A stable manifold is one whose constituent points approach some fixed or periodic point (e.g. points A, B, C or D) as time advances, whereas the points on an unstable manifold approach its fixed/periodic point as time flows backwards. Each of the hyperbolic points in figure 2 has both a stable and an unstable manifold, though the stable manifolds of points A and C and the unstable manifold of point B each have a branch which lies within the ambient air and does not therefore form part of the domain of interest. Following a similar notation to Horner *et al.* (2002), the unstable and stable manifolds of each point will be denoted W_B^u, W_C^s, etc. Under steady conditions, certain branches of the stable and unstable manifolds coincide to produce the separating streamlines
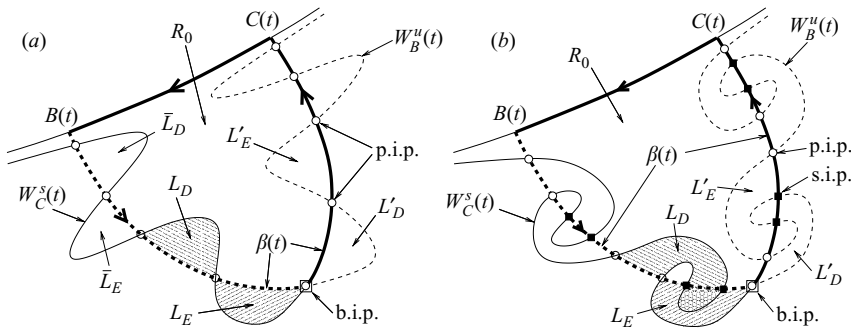
FIGURE 3. Illustration of the tangling of stable and unstable manifolds and the turnstile mechanism of transport into and out of the region R_0 bounded by $\beta(t)$. (*a*) A small-amplitude perturbation, featuring a simple turnstile; (*b*) an example of a self-intersecting turnstile, which is the expected structure when the free surface undergoes a large displacement.

shown in figure 2. As can be seen, the free surface itself is formed from the unstable manifolds associated with points A and C (and the coinciding stable manifold of point B).

When the free surface moves in response to the roll speed modulation, the three fixed points A, B, C become periodic points $A(t)$, $B(t)$, $C(t)$ which move along the free surface but satisfy $A(t+T) = A(t)$ etc. for all t, where T is the modulation period. Likewise, the point $D(t)$ executes a periodic orbit but is not restricted to the free surface. Since the free surface is a material interface, any points on the surface must stay on it as it moves, and so the manifolds $W_B^s(t)$, $W_A^u(t)$ and $W_C^u(t)$ continue to lie along the free surface for all time. However, the stable and unstable manifolds which are not constrained along the free surface will no longer coincide, but will instead intersect (infinitely) many times to form a complicated (yet structured) 'tangle'. Since incompressible velocity fields yield non-dissipative advection equations, tangling of the manifolds occurs for any finite amplitude of the periodic modulation (Summers 1995). An example based on the eddy between points B and C in figure 2(*c*) is shown in figure 3(*a*). Several features of such tangles have been defined in the literature cited above. First, the points at which the manifolds intersect fall into two categories. A 'primary intersection point' (p.i.p.) is one which is connected to $B(t)$ and $C(t)$ by a segment of $W_B^u(t)$ and a segment of $W_C^s(t)$ which do not intersect at any other point. Any other intersection is referred to as a 'secondary intersection point' (s.i.p.). Any of the p.i.p.s can be used to define a time-dependent boundary, $\beta(t)$, of an interior region, R_0, and the chosen p.i.p. is referred to as a 'boundary intersection point' (b.i.p.). In figure 3(*a*), $\beta(t)$ is indicated by the thick lines, and consists of the two segments of $W_B^u(t)$ and $W_C^s(t)$ plus the segment of free surface between $B(t)$ and $C(t)$.

The segments of $W_B^u(t)$ and $W_C^s(t)$ between each pair of adjacent p.i.p.s define a 'lobe' and, as can be seen in the diagram, the lobes lie alternately inside and outside R_0. There are two ways to think about the lobe structure. On the one hand, since the lobes are bounded by invariant manifolds, fluid which lies within a lobe remains within that lobe for all time. Thus, after each period, each lobe moves along $\beta(t)$ from $B(t)$ to $C(t)$ via the b.i.p. However, if one plots the two manifolds at the same stage of each period, they will look the same. Therefore, when viewed periodically, the manifolds and the lobes can be seen as a geometric structure through which fluid flows. For labelling purposes, the latter notion is more useful, since the same label can be applied to whichever lobe occupies a particular region of the domain at a

particular phase of the modulation. For instance, in the pictured example, fluid lying in the interior lobe labelled $\bar{L}_D$ at $t = t_0$ moves to occupy the lobe labelled L'_D at time $t_0 + T$. The parcel of fluid is still bounded by the same segments of $W^u_B(t)$ and $W^s_C(t)$, but the label of the lobe has changed because the lobe now occupies a different position in the manifold structure. Similarly, the exterior lobe $\bar{L}_E \mapsto L_E$. With this in mind, the importance of lobes L_E and L_D can now be seen, because fluid which lies within the exterior lobe L_E will lie within the interior lobe L'_E after one modulation period. Similarly, fluid in the interior lobe L_D will occupy the exterior lobe L'_D. In other words, fluid will be transported into and out of R_0. Only fluid lying in lobes L_E and L_D can enter or leave R_0 and for this reason these lobes are referred to as the entraining and detraining 'turnstile' lobes. Calculating the area of these lobes gives the rate of fluid exchange – see the papers cited above for more detail.

Readers familiar with the oscillating vortex-pair flow considered by (among others) Rom-Kedar *et al.* (1990) and Beigie *et al.* (1994) will note that the eddy between B and C in figure 2(c) and its manifold structure in figure 3(a) are topologically equivalent to one half of the vortex pair. The symmetry of the vortex flow prevents the manifolds lying in the symmetry plane from tangling; these manifolds remain stationary for all time. The equivalent section of R_0 in the present flow is the free surface, which, though composed of stable and unstable manifolds, cannot produce tangling due to its being a material interface. The key difference here is that the free surface is moving inwards and outwards; indeed this is the dominant driving mechanism for fluid transport in the present study. This 'direct' perturbation of the eddy region is potentially capable of producing very large disturbances, and since the eddy region is relatively small (particularly when compared with the open cavity flow of Horner *et al.* 2002), it is possible that fluid which is entrained into R_0 might also be detrained within the same period of modulation, as the free surface returns to its original position. This situation would result in a 'self-intersecting turnstile', as sketched in figure 3(b) – see also Rom-Kedar & Wiggins (1990) or Wiggins (1992). In this case the detraining turnstile lobe overlaps the entraining lobe.

3. Experimental apparatus and method

Experiments were performed on a modified coating rig (Gaskell, Kapur & Savage 2001). This consisted of a high-precision twin-roll apparatus, illustrated in cross-section in figure 1, composed of two stainless steel rolls (labelled C and M for 'constant' and 'modulated') of length $100\,\text{mm}$ and radius $R_C = R_M = R = 25.24\,\text{mm}$, ground to a fine finish of average roughness $r.a. < 0.4\,\mu\text{m}$ and positioned side by side. Each roll is mounted in a precision housing, with a small degree of pre-load applied to the pair of angular bearings to minimize runout. The metering roll and drive are fitted on a horizontal slide enabling the gap, $2H_0$, to be set with feeler gauges to $400 \pm 10\,\mu\text{m}$, accounting for a roll eccentricity within $\pm 5\,\mu\text{m}$. The two rolls are immersed in a bath of fluid so that the fluid level reached the centre of the rolls; this ensured that the system remained 'fully flooded' during the experiments.

Both rolls were driven by (Farnell) DC motors with a 300:1 reduction gearbox and an opto-tachometer interfaced to a computer for direct speed readout. A Hooke's (or 'universal') joint provided a simple and efficient means of modulating the speed of roll M. The drive arrangement is shown in figure 4; the motor is mounted on a pivoted bracket such that the angle, θ, between the driving and driven shafts can be varied between 0 and $75°$. The value of θ determines the magnitude of the perturbation. With reference to figure 4, Ω_C and Ω_D are the (constant) angular velocities of the shafts
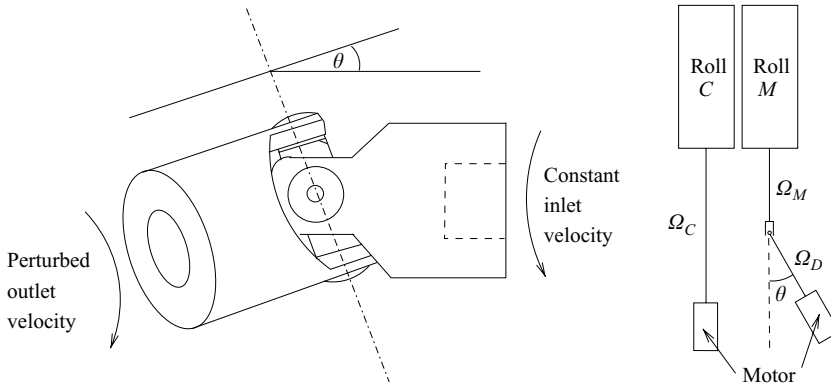
FIGURE 4. The universal (or 'Hooke's') joint used to modulate roll speed, and a plan view of the drive arrangement.
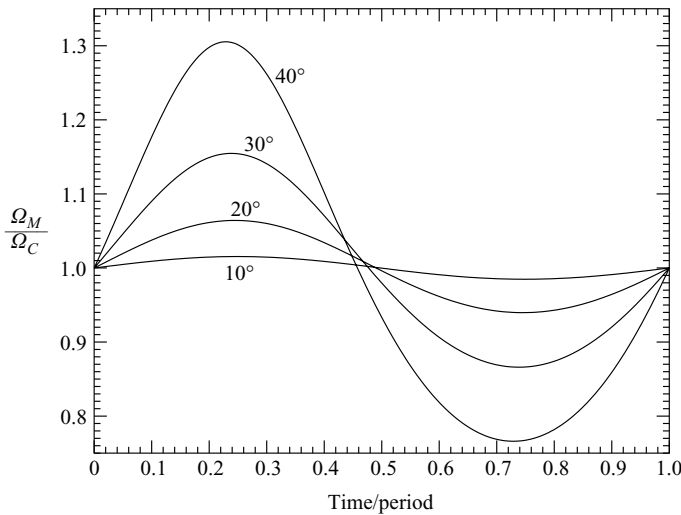

FIGURE 5. The modulation produced by the Hooke's joint inclined at various angles. Note that for ease of comparison, the curves have been shifted along the time axis so that in each case $S = 1$ at time zero.

driven by the two motors, while $\Omega_M(t)$ is the angular velocity of the modulated roll at time t. The speed ratio of the two rolls is given by the formula (Hall, Holowenko & Laughlin 1961)

$$S(t) = \frac{\Omega_M(t)}{\Omega_C} = \frac{\bar{S}\cos\theta}{1 - \sin^2\theta\cos^2\Omega_D t}, \tag{3.1}$$

where $\bar{S} = \Omega_D/\Omega_C$ is the speed ratio of the two motors, which is also the average roll speed ratio. The range of S produced by (3.1) is $\bar{S}\cos\theta \leqslant S \leqslant \bar{S}\sec\theta$, and the frequency of the modulation is $\omega = 2\Omega_D$ since each revolution of the drive shaft produces two complete modulation cycles. Plots of modulations produced using different values of θ with $\bar{S} = 1$ are shown in figure 5, where, for ease of comparison, the phase shift

$$\Omega_D t = \frac{1}{\bar{S}}\arccos\frac{(1 - \cos\theta)^{1/2}}{\sin\theta}$$

$R = 0.02524\,\mathrm{m}$	$\rho = 860\,\mathrm{kg\,m^{-3}}$	$Re = 0.021$
$H_0 = 2 \times 10^{-4}\,\mathrm{m}$	$\mu = 0.7\,\mathrm{Pa\,s}$	$Sr = 0.028$
$L = 2.247 \times 10^{-3}\,\mathrm{m}$	$\gamma = 0.03\,\mathrm{N\,m^{-1}}$	$Bo = 1.420$
$U_C = 7.5 \times 10^{-3}\,\mathrm{m\,s^{-1}}$	$\omega = 0.594\,\mathrm{rad\,s^{-1}}$	$Ca = 0.175$

TABLE 1. Summary of dimensional and dimensionless parameters corresponding to the experimental conditions. The working fluid is a high-viscosity oil.

has been applied so that $S = 1$ at $t = 0$ in each case. For small θ, the response is approximately sinusoidal, as confirmed by a Maclaurin expansion of (3.1), which gives $S = \bar{S}(1 + \frac{1}{2}\theta^2 \cos \omega t + O(\theta^4))$. However, as θ increases, a distinct asymmetry is visible in the response.

The evolution of the flow within the bead of fluid was highlighted using dye injection. A small hypodermic needle was mounted in a clamp above the free surface. The clamp was in turn mounted on a piece of spring steel so that by pressing gently on the housing the tip of the needle could be inserted into the fluid through the free surface. Prior to injection, a pendant drop was formed on the end of the needle to minimize the duration of the disturbance to the flow.

The fluid bead was visualized using a CCD camera (Panasonic 0.08 lux model WV-BP310B) attached to a monocular zoom microscope (Meiji Techno Company). A transparent end plate was fitted flush to the end of the rolls to prevent curvature of the fluid meniscus distorting the flow field, and the microscope was focused some 5 mm from the edge of the roll to minimize distortions due to three-dimensional flow in the vicinity of the end plate (Gaskell, Innes & Savage 1998a). The bead was lit using a halogen light source fitted with twin fibre-optic light guides (Olympus Highlight 3000), the image was recorded onto S-VHS video tape and captured in digital format using a Silicon Graphics INDY workstation. A list of the fluid properties and other parameters corresponding to the experimental conditions is given in table 1.

4. Computational method

4.1. *Governing equations*

The liquid is taken to be Newtonian, with constant and uniform viscosity, μ, density, ρ, and surface tension, γ. The ambient air is assumed to be inviscid with constant pressure, and its flow is therefore not modelled here; the ambient pressure merely provides a datum from which to measure the liquid pressure. A suitable length scale for the problem is given by $L = \sqrt{RH_0}$, which has been used before in lubrication analysis (Pitts & Greiller 1961), but is also roughly the length of the recirculation region for the physical parameter values considered. The velocity scale is $U = U_C = \Omega_C R$, the peripheral speed of the constant-speed roll. Scaling pressure by $\mu U/L$ and time by the modulation period, $T = 2\pi/\omega$, leads to the following dimensionless form of the Navier–Stokes and continuity equations:

$$Re\,(Sr\dot{\boldsymbol{u}} + \boldsymbol{u} \cdot \nabla \boldsymbol{u}) = -\nabla p + \nabla^2 \boldsymbol{u} + (Bo/Ca)\hat{\boldsymbol{g}}, \qquad (4.1)$$

$$\nabla \cdot \boldsymbol{u} = 0, \qquad (4.2)$$

where p is pressure, $\boldsymbol{u} = (u, v)$ is velocity, $\dot{\boldsymbol{u}} = \partial \boldsymbol{u}/\partial t$, $\hat{\boldsymbol{g}}$ is a unit vector in the direction of gravity, and the Reynolds, Strouhal, Bond and capillary numbers are

given respectively by

$$Re = \frac{\rho U_C L}{\mu}, \quad Sr = \frac{L}{U_C T}, \quad Bo = \frac{\rho g L^2}{\gamma}, \quad Ca = \frac{\mu U_C}{\gamma}. \quad (4.3)$$

The experimental values of these dimensionless groups are given in table 1.

4.2. *Finite element method*

Motivated by the success and prevalence of the finite element (FE) method in modelling steady-state coating flows, a time-dependent implementation of the technique is adopted here. The formulation employed is a Galerkin weighted residual approach based on that described in detail for steady free-surface flows by Kistler & Scriven (1983). The computational mesh is constructed in the same way as that of Coyle *et al.* (1986), but with more elements to provide the necessary resolution of the velocity field (Souvialotis, Jana & Ottino 1995). Six-node triangles instead of quadrilaterals are also chosen to facilitate the tracking of passive tracer trajectories through the mesh.

On each element, the velocity and pressure are represented in terms of nodal quantities by means of biquadratic (Q_j) and bilinear (L_k) interpolation functions, i.e.

$$\boldsymbol{u}(\xi, \eta) = \sum_{j=1}^{6} \boldsymbol{u}_j Q_j(\xi, \eta), \qquad p(\xi, \eta) = \sum_{k=1}^{3} p_k L_k(\xi, \eta), \quad (4.4)$$

where $\boldsymbol{u}_j$ and p_k are the nodal values, and (ξ, η) are local coordinates defined on a 'standard' element which is mapped into each physical element. The free surface is parameterized using a set of linear 'spines' having known but adjustable base points and orientations, with the position of each mesh node on the free surface given by its distance, h_i, along a spine from the spine's base point (Kistler & Scriven 1983). The base points lie either on a roll surface or on a special spine connecting the roll surfaces (see Coyle *et al.* 1986), and the unknown distances h_i – usually referred to as 'heights' – are determined by application of the kinematic condition along the free surface (see below).

Since the modulations considered here are slow, and therefore temporal gradients in $\boldsymbol{u}$, p and h_i are small, a backward Euler scheme is sufficient to discretize time derivatives. At each timestep the nonlinear algebraic weighted residual equations are solved for updated spine heights and nodal values of $\boldsymbol{u}$ and p by Newton iteration. Note that since the computational mesh moves in response to the free-surface motion, the material derivative in the weighted residual form of (4.1) must be modified to account for the relative motion of the liquid and the mesh (Jimack & Wathen 1991). Hence, in discretized form, (4.1) becomes the following momentum residual equation:

$$\int_\chi [Q_j Re(Sr\dot{\boldsymbol{u}} + (\boldsymbol{u} - Sr\dot{\boldsymbol{x}}) \cdot \nabla \boldsymbol{u}) + \nabla Q_j \cdot \boldsymbol{\sigma} - Q_j (Bo/Ca)\hat{\boldsymbol{g}}] \, \mathrm{d}\chi - \int_{\partial \chi} Q_j \hat{\boldsymbol{n}} \cdot \boldsymbol{\sigma} \, \mathrm{d}s = 0 \quad (4.5)$$

where $\boldsymbol{\sigma}$ is the dimensionless stress tensor with components $\sigma_{\alpha\beta} = -p\delta_{\alpha\beta} + \partial u_\alpha/\partial x_\beta + \partial u_\beta/\partial x_\alpha$, $\hat{\boldsymbol{n}}$ and s are the unit normal to and arclength along the boundary, $\partial\chi$, of the domain, χ, and $\dot{\boldsymbol{x}} = \sum \dot{h}_i \partial \boldsymbol{x}/\partial h_i$ is the mesh velocity. Typically 3 or 4 iterations are required to reduce the L_2 norm of the residuals to below 10^{-10} at each timestep. As explained in the next section, the FE system must be solved over two modulation periods, and so the largest acceptable timestep size was determined by repeating the computations with successively halved timesteps until the nodal velocities and free-surface positions calculated using the two smallest timesteps differed by less than

$10^{-3}\%$ after two modulation periods. The larger of these two timesteps was then taken to be the largest acceptable timestep.

The boundary conditions imposed are as follows. On the roll surfaces, the no-slip condition yields

$$\boldsymbol{u} = \hat{\boldsymbol{t}} \text{ on roll } C, \quad \boldsymbol{u} = S(t)\hat{\boldsymbol{t}} \text{ on roll } M, \tag{4.6}$$

where $\hat{\boldsymbol{t}}$ is the unit tangent to the appropriate surface. On the free surface the tangential stress vanishes, while the normal stress is balanced by surface tension. Taking pressure to be relative to the ambient pressure, these conditions are encapsulated in the natural boundary condition

$$\hat{\boldsymbol{n}} \cdot \boldsymbol{\sigma} = \frac{1}{Ca}\frac{\mathrm{d}\hat{\boldsymbol{t}}}{\mathrm{d}s}, \tag{4.7}$$

which is convenient for insertion into (4.5). As discussed in §2, the free surface is a material interface, and therefore fluid may not cross it. This fact leads to the kinematic condition

$$(\boldsymbol{u} - Sr\dot{\boldsymbol{x}}_{\mathrm{fs}}) \cdot \hat{\boldsymbol{n}} = 0, \tag{4.8}$$

where $\boldsymbol{x}_{\mathrm{fs}}$ represents the coordinates of a point on the free surface. Following the usual Galerkin approach, equation (4.8) is weighted by Q_j and integrated over the free surface to provide the equations which determine the spine heights at a given timestep.

The outflow planes are prescribed to be perpendicular to the rolls, and the 'free boundary condition' of Papanastasiou, Malamataris & Ellwood (1992) is used to allow for the changes in film thickness and flow rate resulting from the modulation of roll speed. This approach simply involves calculating the boundary integral in (4.5) as it stands, using the current values of u, v, p and h along the outflow planes. (Note that for this integral, $\hat{\boldsymbol{n}}$ refers to the normal to the outflow plane.)

Finally, the inlet boundary is positioned at $y = 0$, the point of minimum separation between the roll surfaces. Diffusion of momentum across this narrow gap is assumed to be very rapid, such that the flow rate adjusts instantaneously to changes in roll speed but the form of the velocity profile remains the same. Hence, following Coyle *et al.* (1986), the velocity at the nip is derived from lubrication theory:

$$v(\alpha, t) = \tfrac{3}{4}[1 + S(t) - 2\lambda](\alpha^2 - 2\alpha) + \tfrac{1}{2}(S(t) - 1)\alpha + 1. \tag{4.9}$$

Here λ is the dimensionless flow rate through the nip, and α is a transformed x coordinate such that $\alpha = 0$ on the surface of roll C and $\alpha = 2$ on roll M (Coyle *et al.* 1986). Since λ is unknown *a priori*, it must be determined as part of the finite element solution, and this can be achieved using the lubrication prediction for the pressure at the nip:

$$p = \frac{3\pi}{16\sqrt{2}}[2(S(t) + 1) - 3\lambda] + \frac{BoR}{CaH_0}y_{\mathrm{bath}}, \tag{4.10}$$

where y_{bath} is the position of the surface of the bath in which the rolls lie (in this study $y_{\mathrm{bath}} = 0$ since the rolls are half-submerged). Equation (4.10) is coupled to the FE system by replacing its left-hand side by the average of the nodal pressures at the nip (Coyle *et al.* 1986).

4.3. *Calculation of passive tracer trajectories*

Central to the visualization and analysis of transport in modulated flows are the trajectories of passive tracer particles, which provide a means of observing fluid motion without influencing the flow. The trajectory, $\boldsymbol{x}(t)$, of a tracer is found by

integrating the advection equation,

$$\frac{\mathrm{d}\boldsymbol{x}}{\mathrm{d}t} = \boldsymbol{u}(\boldsymbol{x}, t)/Sr, \qquad (4.11)$$

which is here achieved using a fourth-order Runge–Kutta scheme. Large collections of passive tracers form the computational equivalent of a dye blob in an experiment, and hence offer the potential for direct comparison between simulations and experiments. Note that molecular diffusion is neglected here: the time scale for this effect to be noticeable is assumed to be much larger than the modulation period (as borne out by experimental observations). Since evaluation of the velocity field is computationally expensive, for periodic flows it is desirable to decouple the trajectory calculations from the calculation of $\boldsymbol{u}(\boldsymbol{x}, t)$, thus allowing velocity data from just one period of the modulation to be re-used in the integration of (4.11) over many periods. This does however raise the question of how to interpolate between the available 'snapshots' of the velocity field to obtain $\boldsymbol{u}$ at arbitrary times.

In the baffled cavity flow mentioned earlier, Jana *et al.* (1994) used the boundary element method and took advantage of its low memory requirements to store in arrays the boundary information corresponding to several intermediate positions of the moving baffles. They were able to do this because the motion of the baffles was prescribed, and hence appropriate fluid velocities could be set at the moving surfaces. This is not possible in the present problem since the free-surface position, shape and motion in response to the modulation are not known in advance.

Anderson *et al.* (2000*b*) studied a cavity flow in which fluid inertia could not be ignored. They therefore had to use a numerical method to determine $\boldsymbol{u}(\boldsymbol{x}, t)$ and chose the spectral element method for this. The result was a finite sequence of instantaneous (unsteady) flow fields corresponding to different times. From this set, the flow field at intermediate times was found using linear interpolation between consecutive solutions, i.e. $\boldsymbol{u}(\boldsymbol{x}, t_i)$ and $\boldsymbol{u}(\boldsymbol{x}, t_{i+1})$. A similar approach was adopted by Nishimura & Kunitsugu (1997), who used the finite element method. They pre-calculated and stored all the nodal velocity values required for each timestep throughout one period. For a recent evaluation of such interpolation methods, see Mancho, Small & Wiggins (2006).

Here, an alternative means of temporal interpolation is employed. Since the perturbation of the roll speed (3.1) is periodic and continuous, trigonometric polynomials are a natural choice for interpolating between consecutive (unsteady) velocity field solutions. This approach was suggested by Rosenfeld (1995, 1996), motivated by the need for dramatic reductions in data storage requirements to allow interactive calculations of streaklines for flow visualization. Though shown to be very effective for the vortex-shedding flow past a cylinder and a pulsed flow through a constricted channel, the method seems not to have been used in chaotic advection studies.

In order to synthesize a finite element solution at arbitrary time t, one period of the modulation is first 'sampled' by calculating FE solutions at N uniformly spaced values of t throughout the period, i.e. at $t_j = j/N$, $j = 1, \ldots, N$. Any nodal or spinal quantity, ϕ (representing u, v, p, h, etc.), can then be expressed approximately as a truncated Fourier series,

$$\phi_k(t) = \tfrac{1}{2}a_0^{\phi_k} + \sum_{m=1}^{M} \left\{ a_m^{\phi_k} \cos 2\pi mt + b_m^{\phi_k} \sin 2\pi mt \right\}, \qquad (4.12)$$

where k refers to a particular node or spine, M is the number of terms in the series, and the coefficients, determined by a least-squares procedure, are given by (e.g.

Mathews 1992)

$$a_m^{\phi_k} = \frac{2}{N} \sum_{j=1}^{N} \phi_k(t_j) \cos 2\pi m t_j \qquad \text{for } m = 0, 1, \ldots, M, \qquad (4.13a)$$

$$b_m^{\phi_k} = \frac{2}{N} \sum_{j=1}^{N} \phi_k(t_j) \sin 2\pi m t_j \qquad \text{for } m = 1, 2, \ldots, M. \qquad (4.13b)$$

In the above, $\phi_k(t_j)$ represents the value of quantity ϕ at node/spine k in the FE solution corresponding to time t_j. The coefficients $a_m^{\phi_k}$ and $b_m^{\phi_k}$ are calculated for each nodal velocity and each spine height in the finite element mesh; the node coordinates (x_k, y_k) are not interpolated directly because it was found to be more efficient to interpolate the (far fewer) spine heights and then reconstruct the mesh from these as required.

Each new computation to determine the coefficients $a_m^{\phi_k}$ and $b_m^{\phi_k}$ begins from the corresponding steady-state solution with speed ratio equal to $\bar{S}$. Hence there is always a short transient as the flow accelerates from this state to the modulated state, and so the recording of FE solutions to calculate $a_m^{\phi_k}$ and $b_m^{\phi_k}$ cannot begin immediately. For the small values of Re considered here, it was found that one complete period of modulation was ample time for the initial transients to decay and for a periodic state to be established. Therefore the summations (4.13a, b) began in the second period of modulation. Since there is a phase lag between the roll speed modulation and that of the free-surface position, and since this is dependent on $\bar{S}$, θ, Re and ω, the phase, ζ, of all modulations is for convenience defined with respect to the position of the 'tip' of the meniscus, i.e. the lowest point on the free surface, such that $\zeta = 0$ when the meniscus tip is closest to the nip.

Figure 6 shows example variations of velocity and spine height and the corresponding interpolation via (4.12). The accuracy with which (4.12) captures the behaviour of the FE system depends on both the number of terms in the series, which governs the complexity of the behaviour that can be represented, and the number of sample points t_j used to determine $a_m^{\phi_k}$ and $b_m^{\phi_k}$. It was found that the velocity components at nodes close to stagnation points produced the most complex nonlinear response to the modulation, see figure 6(c, d), but even these were well represented by series of just $M = 6$ terms, as can be seen by the close agreement in figure 6. While a minimum of $2M + 1$ sample points is needed to calculate the coefficients in (4.13), the accuracy of (4.12) improves as N increases. In the results presented here, each timestep of the FE system is used as a sample point, and $N = 1000$ was found to give both a suitable timestep size (see §4.2) and excellent agreement between (4.12) and the FE data.

5. Results

5.1. *Evolution of a dye blob*

Figure 7 presents a comparison of experimental flow visualization and a corresponding simulation of a blob of dye injected into the flow. In this flow, $\bar{S} = 1$ and $\theta = 30°$ and the other parameters are as in table 1. Since it is very difficult to inject dye into the domain without disturbing the flow, the initial points comprising the simulated blob were determined from the position and shape of the real dye blob about one second after its injection – this is shown in the top left image in figure 7. The GNU Image Manipulation Program was used to blank out everything in the image except the dyed
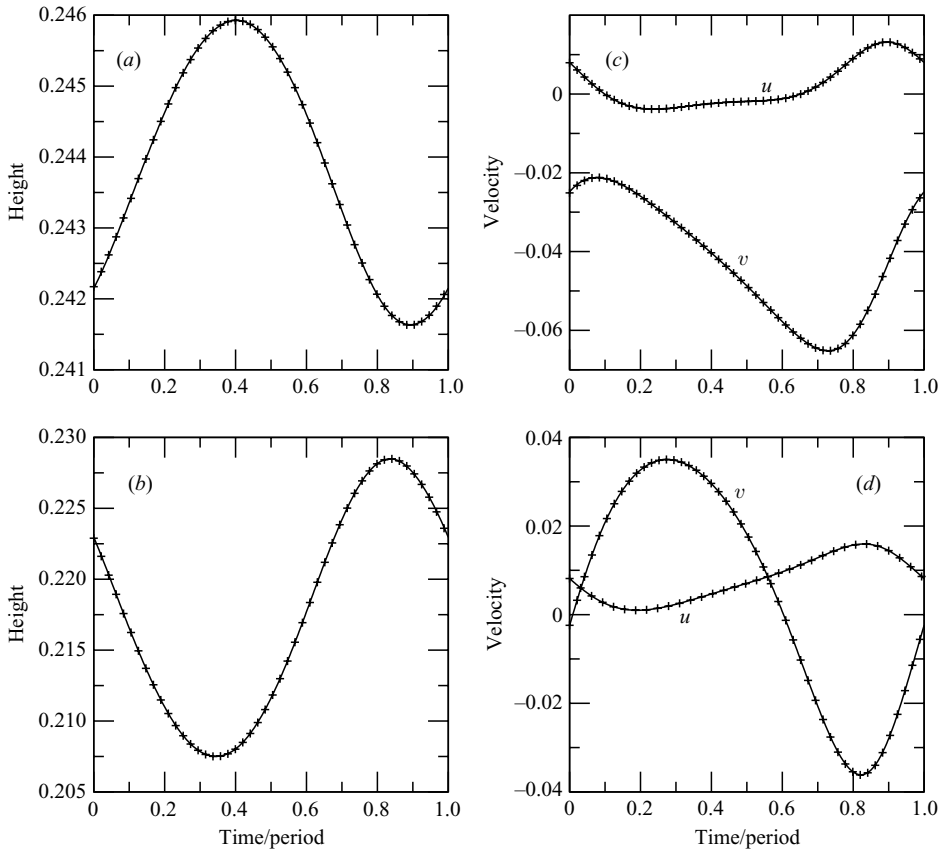
FIGURE 6. Illustrations of the response of the finite element system and the corresponding trigonometric polynomials to a Hooke's joint modulation with $\theta = 40°$. The FE data are shown as $+$ and the interpolated values as solid lines. Note that for reasons of clarity, not all the FE data points have been plotted. (*a*) Height of a spine close to the meniscus tip location; (*b*) height of a spine with base on the modulated roll; (*c*) and (*d*) show horizontal, u, and vertical, v, velocity components at two nodes close to the interior saddle point.

fluid, and the resulting image was then saved in (ASCII) PNM format, from which it is straightforward to convert each pixel into an initial point in (x, y) space. This collection of over 17 000 points was then advected forward in time using equations (4.11). The phase at the time of injection was checked by observing the rotational angle of the pins in the Hooke's joint relative to the plane defined by the two shafts.

In the experiments, dye tends to linger on the free surface close to point *B* (see figure 2) and is continuously drawn into the domain, creating a streak down the centre of the eddy region. The mathematical (continuum) description of the flow does not allow for this behaviour (see §2), so to mimic the effect in the simulation a fresh tracer is added to the domain close to point *B* at each timestep. This enables a better judgement of the accuracy of the simulation with respect to the experiments, by revealing more of the structure of the flow.

The overall visual agreement between the simulation and the experiment is excellent: the simulation captures the winding effect of the right-hand eddy, the movement of the interior saddle point, and the ejection of fluid along the free surface. The only difference in the evolution of the blob is in the thin filament of dye which skirts
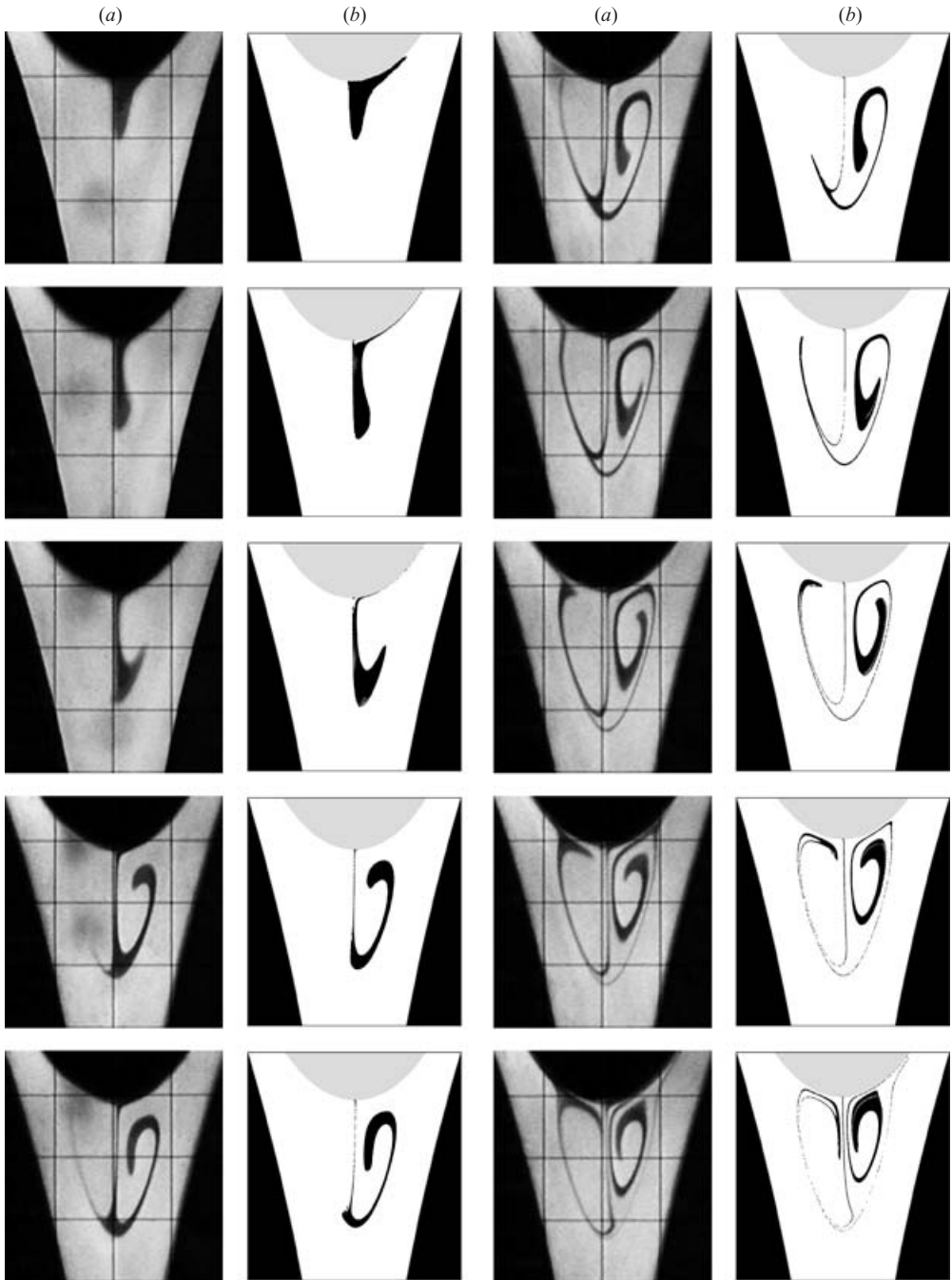
FIGURE 7. Comparison of simulation (*b*) with experiment (*a*) for the evolution of a dye blob dropped onto the free surface. Time increases in steps of 1 s in the vertical sense. The period of modulation is 10.57 s, so the images illustrate a little under one period. The phase in the top left image is 0.78, and the Hooke's joint is set at 30° with $\bar{S} = 1$, giving the range $0.866 \leqslant S \leqslant 1.154$.
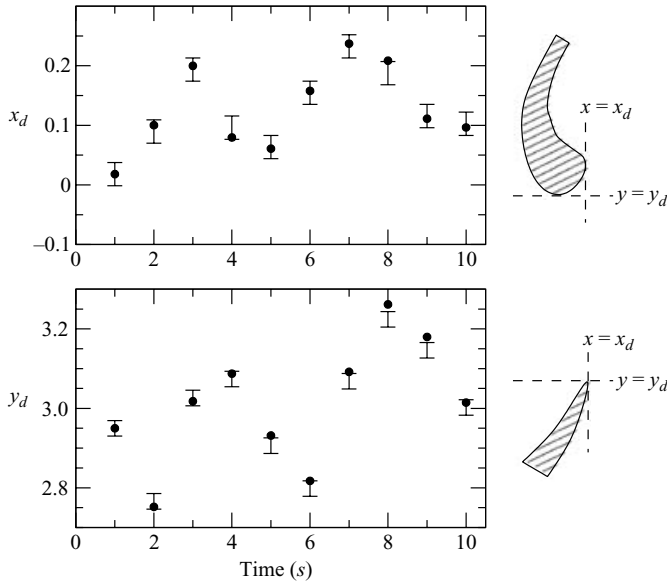
FIGURE 8. A quantitative comparison of the results presented in figure 7. The plots show the position of the advancing front of the dye blob as it winds around the right-hand eddy. The co-ordinates x_d and y_d represent the positions of tangents to the dye blob as illustrated in the schematics on the right. The predictions of the simulation are shown as black circles and the experimental data as error bars.

the left-hand eddy before the main strand of ink follows – the simulation shows the movement of the main strand, but does not feature the preceding dilute filament. This is attributed to very slight errors in picking out the edges of the initial blob from the greyscale image, i.e. there was a little ink at the boundary of the blob which was not captured and converted into initial points for the simulation. Other comparisons with repeated dye injection experiments at different phases show a similar agreement.

A more quantitative comparison of the simulation and experiment is given in figure 8, where the position of the leading front of the dye blob in the right-hand eddy is plotted against time. To avoid trying to locate a single point on the curved blob edge, the position is represented by two tangents as indicated in the sketches on the right of figure 8. The values x_d and y_d are dimensionless (scaled by $L = \sqrt{RH_0}$ – see table 1) and refer to the coordinate system indicated in figure 1. The experimental values are found from the still images, and the error in identifying the edges of the blob is estimated as ± 2 pixels. Again, good agreement is seen, especially between the x_d values.

5.2. *Visualization of fluid exchange*

Having established that the numerical simulation provides a true representation of the flow, figure 9 shows a sequence taken from a simulation which illustrates the fluid exchange process for the case $\bar{S} = 1$ and $\theta = 30°$. For convenience, the steady-state streamlines corresponding to $S = 1$ were used to define the eddy region. This region was 'seeded' with tracers by constructing a uniform square grid of points extending beyond the boundaries of the eddies, and then using the streamfunction to determine which points lay inside each eddy. Discarding those points outside the eddy region left about 60 000 tracers initialized inside the area of interest. The simulation was

FIGURE 9. Numerical simulation of approximately 60 000 points initially uniformly spaced (via a square grid) within the steady-state (symmetric) recirculation zone corresponding to $\bar{S} = 1$. The phase increases in steps of 0.1 from 0.275 at (*a*). The Hooke's joint angle was 30°, giving *S* as in figure 7.

then started at a phase (slightly greater than 0.25) at which the free-surface tip location matched that in the steady state. At this phase, the free surface is moving outwards, and as it does a finger of fresh fluid is drawn into the eddy region along the free surface from the right (figure 9*a–c*; see also figure 10 for an experimental visualization). For easy reference later, this strand of fresh fluid is designated E_1. A much smaller quantity of fluid also enters from the left – again along the free surface. When the meniscus reaches its maximum extent and starts to recede again, fluid is ejected from the eddy region along the free surface towards the modulated (right-hand) roll (figure 9*d–g*). At this stage, the speed of the modulated roll is increasing, and hence the right-hand film is increasing in thickness at the expense of the left-hand film. This asymmetry produces a smaller ejection to the left along the free surface a little later than the main ejection.
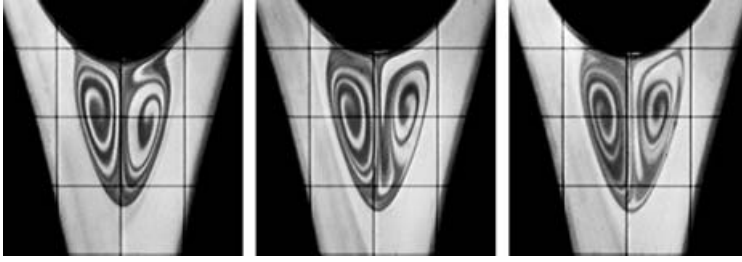
FIGURE 10. Experimental images showing the incursion of fluid into the recirculation region as the free surface moves outward. A 'finger' of fluid enters from right to left between the right-hand eddy and the free surface, and is then drawn down the centre of the recirculation zone. Once again, $\theta = 30°$ and $\bar{S} = 1$.

While fluid originally within the eddy region is being ejected, the fresh fluid E_1 travels around the right-hand eddy such that at the beginning of the next modulation cycle it lies ahead of the second influx of fresh fluid (figure $9h, i$), designated E_2. As a result, when E_1 reaches the bottom of the eddy region, the interior saddle point D (figure 2) is in such a position that E_1 is split between the left- and right-hand eddies (figure $9l$). When the right-hand portion of E_1 reaches the free surface again it is further split, with some of it leaving the eddy region (figure $9n$). The snapshots in figure $9(o)$ and (p) indicate that when the free surface moves inwards again (for the second time), much of the fresh fluid E_2 is ejected to the right. This would also have been seen with blob E_1 if the simulation had started at phase $\zeta = 0$ rather than part way through the outward stage of the free-surface movement.

An alternative means of visualization is to inject tracers into the flow upstream of the eddy region and observe how they enter that part of the domain. This is done in figure 11, in which a fresh line of tracers is initiated at the same upstream location at each timestep of the simulation. The result is a continuous stream of dyed fluid rather like the experiments described by Horner *et al.* (2002). The flow conditions in figure 11 match those in figure 9, and certain features, such as the entrainment from the left, are shown up more clearly in this way. This method also captures the complete E_1 entrainment, and shows via plots $(e–g)$ that much of the entrained fluid is subsequently lost. This is in keeping with the self-intersecting turnstile mechanism mentioned in §2, and will be explored further in the next section.

By way of comparison, figure 12 uses the same method of visualization as figure 11, but shows the behaviour when $\bar{S} = 1.5$ (with θ remaining at $30°$). In this case the steady-state flow corresponding to the instantaneous value of S is always topologically identical to that in figure $2(c)$. As before, the stream of dye splits as it encounters the unstable manifolds of the interior saddle point D, and the fluid on the left follows the path of the 'transfer-jet' between the two eddies in figure $2(c)$. When this stream of fluid reaches the free surface on the right-hand side of the eddy region, a very small portion of it continues out into the right-hand film, but most is entrained into the right-hand eddy, along with some of the fluid which was originally in the left-hand eddy and a substantial influx of fluid from the right-hand dye stream. Dyed fluid travelling down the middle of the eddy region then enters the left-hand eddy, and the cycle of entrainment and detrainment continues. Comparing figures 11 and 12, one can see from the greater presence of black within the eddy region of figure 12 that more fluid is exchanged when $\bar{S} = 1.5$ than when $\bar{S} = 1$.
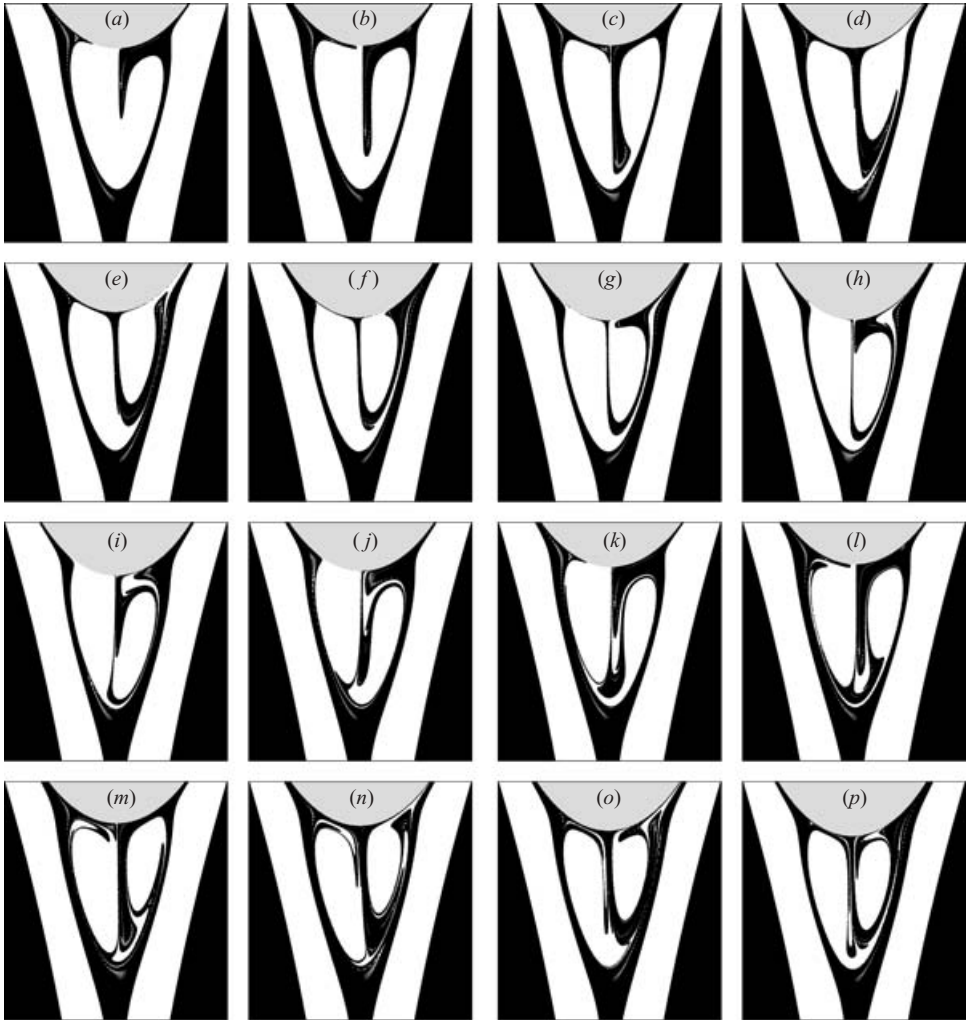
FIGURE 11. Numerical simulation of a continuous source of tracers located upstream of the eddy region. The flow conditions are as in figure 9.

A simple means of providing a more quantitative comparison of fluid exchange rates is to repeat the seeded-eddy simulation of figure 9 and plot the number of tracers remaining in the domain as a function of time. This is done in figure 13, which is similar to the concentration plots presented by Rom-Kedar & Poje (1999). In each curve the detrainment of fluid from the eddy region shows as a drop in the tracer 'population', and each entrainment phase as a flat plateau (since there are no tracers in the fresh fluid). Note that the plot gives the percentage of initial tracers remaining within the domain rather than in the eddy region, since the end of the domain is easier to define. This affects the results only by introducing a short time lag between a particle leaving the eddy region and subsequently leaving the domain after travelling within one of the films. The curves in figure 13 show a similar behaviour to those obtained experimentally by Wierschem & Aksel (2004), who used an average greyscale value to indicate the loss of fluorescent tracer from an eddy.

This may seem to be a fairly crude method of comparison, since no account is taken of any connectivity between tracers, and therefore the volume of fluid exchanged is

FIGURE 12. As figure 11, but for the asymmetric case $\bar{S} = 1.5$. The Hooke's joint remained
at angle $\theta = 30°$, giving $1.299 \leqslant S \leqslant 1.725$.

not directly measured. However, several fixed rectangular regions were set up in the
core of each eddy in order to monitor the density of tracers over time. This was
found to remain practically constant throughout each simulation, suggesting that the
number of tracers left in the domain (i.e. once the tracer population curves have
levelled out) is a reasonable indication of the volume of fluid which was not expelled
from the eddies. By comparison with the initial state, this in turn indicates the relative
volumetric transport rates out of the recirculation zone.

In most of the curves in figure 13 the first decrease in tracer population is much
larger than the rest, and this is consistent with the theoretical results of Rom-Kedar &
Poje (1999), who showed that for low-frequency periodic perturbations almost all fluid
which is entrained into a recirculation during each period is detrained in the following
period. Hence when observing a system in which all the fluid in the recirculation region
is dyed at some time t_0, most of the dyed fluid which can be transported out of a
recirculation region is transported in the first period from t_0. This behaviour is
certainly seen for the $\bar{S} = 1.5$ curves in figure 13. In fact, as described above, much of
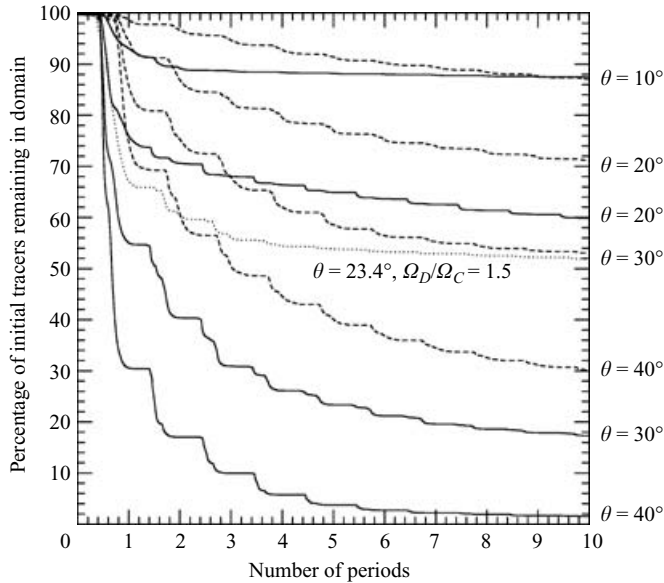
FIGURE 13. Percentage of initial points remaining inside the domain as a function of time for different Hooke's joint angles, θ: - - -, $\bar{S} = 1$; ——, $\bar{S} = 1.5$. The additional dotted line gives the response when $\bar{S} = 1.5$ and θ is adjusted to give a free-surface response with the same amplitude as the $\theta = 30°$ case.

the fluid which is entrained in one period is detrained during the same period. This is a consequence of the relatively large amplitude and low frequency of the perturbation produced by the free-surface movement. The reason why the $\bar{S} = 1$ curves do not exhibit quite the same difference between the first and subsequent periods is partly that in this case there is fluid exchange between the two eddies which make up the recirculation zone. Hence, some of the fluid entrained and detrained in each period is made up of fluid transferred between the eddies, which does not change the population of tracer particles within the domain. However, there is also a modulation frequency difference between the two cases, and the difference in speed of the modulated roll affects the orbital frequency of fluid within the eddies. Modulation frequency has a strong influence on the transport rates, and is discussed in more detail later.

In each case presented in figure 13 the rate of tracer loss decreases over time, such that the curves level off. This indicates that an unmixed core remains in the eddy region. In fact there are two cores, which – as is to be expected – surround the elliptic stagnation points at the heart of each eddy. Figure 14 shows the positions of the tracers after 10 periods of modulation with $\theta = 30°$. For comparison, the steady-state streamlines corresponding to the extremes of speed ratio are overlaid. Note that the tracers are plotted at phases for which the meniscus tip position matches that in the unperturbed steady case. Note also that the plots are not to the same scale, which is why the tracers in figure 14(b) appear less densely distributed. As can be seen in figure 13, after 10 periods the population curves have not quite levelled out completely, and so there are still some tracers (noticeably in the free-surface eddy in figure 14b) which are orbiting the core and which will gradually work their way out into the film. However, the shapes of the cores are easily distinguished.

From the results of figure 13, the asymmetric case, $\bar{S} = 1.5$, appears to be much more amenable to transport enhancement by speed modulation, with almost all the
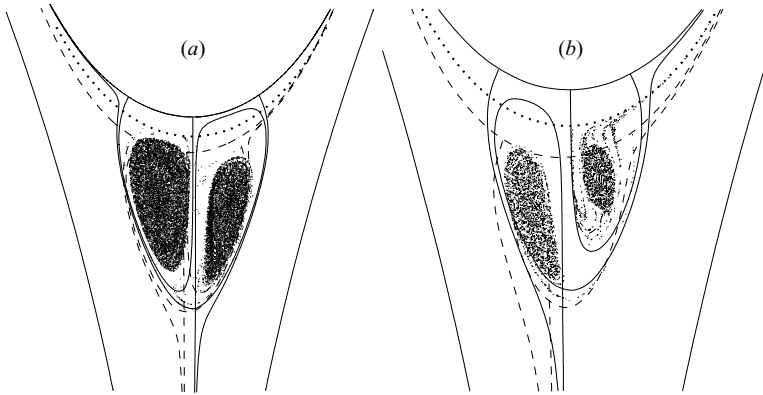
FIGURE 14. Positions, after 10 modulation periods, of tracers which were initially spread uniformly (on a square grid) through the eddy region. The corresponding free-surface position is shown as a dotted line. The overlaid streamlines represent the steady states corresponding to the extremes of speed ratio produced by the Hooke's joint modulation. The dashed and solid lines refer respectively to the maximum and minimum speed ratio solutions in each case. (a) $\bar{S} = 1$ and (b) $\bar{S} = 1.5$, with $\theta = 30°$ in each case.
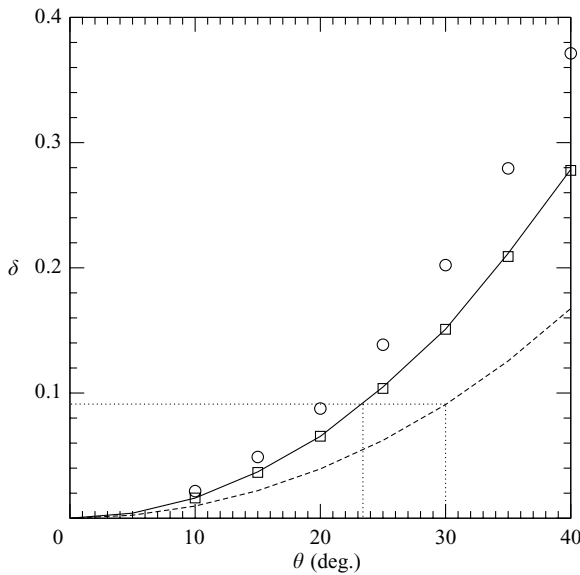

FIGURE 15. Effect of the Hooke's joint angle, θ, on the dimensionless amplitude of the free-surface response, δ, as calculated from the movement of the meniscus tip: - - -, $\bar{S} = 1$; ———, $\bar{S} = 1.5$. For comparison, the additional data points give the difference in free-surface tip position between steady-state solutions corresponding to the extremes of S produced by each θ for $\bar{S} = 1$ (squares) and $\bar{S} = 1.5$ (circles). Note that it is merely coincidence that the squares should lie on the solid curve.

initial tracers evacuated after 10 periods at a Hooke's joint angle of 40°. This picture is deceptive, however, because one must take into account the response of the free surface to the speed modulation. For a given shaft angle, increasing $\bar{S}$ increases the range of speed ratio produced by (3.1), which in turn produces a larger amplitude, δ, in the free-surface movement. Note that δ as used below is a dimensionless quantity, and is scaled by $L = \sqrt{RH_0} = 2.247 \times 10^{-3}$ m (see also table 1). Figure 15 plots the

amplitude of the free-surface response as a function of θ for the two mean speed ratios $\bar{S} = 1$ and 1.5. For comparison the graph also includes (as discrete symbols) the difference in the meniscus tip position found by comparing the steady-state solutions corresponding to the extremes of S produced by several Hooke's joint angles. (Note that the latter results for $\bar{S} = 1$ appear to lie on the solid curve corresponding to $\bar{S} = 1.5$, but this is purely coincidental.) For each $\bar{S}$ the transient response of the free surface is rather less than the difference between the steady states, indicating that a quasi-steady approach would not give a true representation of the flow, even at the small modulation frequency used here. Figure 15 also illustrates how two different values of θ could be chosen to give the same δ at the two speed ratios. The effect of this compensation on the rate of tracer loss is given in figure 13 as the dotted curve, which shows that after 10 modulation periods, a similar percentage of tracers remains in the domain. Initially the rate of tracer loss is much greater for the $\bar{S} = 1.5$ case, though, due to the much smaller transfer of fluid between the eddies in the asymmetric flow.

5.3. *Mechanism of fluid exchange*

The above visualizations and descriptions can be made clearer by calculating and observing the invariant manifolds discussed in §2. By way of example, this is done here only for the eddy attached to the free surface in the $\bar{S} = 1.5$ case. Similar plots can be constructed for the interior eddy. Figure 16 shows one period of the modulation produced by a drive shaft angle of 20°, and presents the unstable manifold associated with point B, W_B^u, and the stable manifold of point C, W_C^s. The manifolds are calculated by inserting at each timestep a new passive tracer positioned very close to the relevant periodic orbit in the direction of the appropriate manifold. The tracers are then advected forwards or backwards in time as appropriate to form the invariant manifolds.

Figure 16(a) corresponds to a phase of $\zeta = 0$, at which the free surface is at its lowest position and the recirculation region, R_0, is at its smallest. For clarity, only the minimum length of the unstable manifold is shown, but W_C^s represents the evolution over several periods. The primary intersection points (p.i.p.s) of the two manifolds (see §2) are indicated by small open circles, and the one nearest C in figure 16(a) forms the boundary intersection point (b.i.p.). The boundary of R_0 is composed of the segment of W_C^s connecting C to the b.i.p., the segment of W_B^u connecting B to the b.i.p., and the segment of the free surface connecting B and C. The entraining turnstile lobe, L_E, is bounded by the segments of W_B^u and W_C^s between the b.i.p. and the next p.i.p. along W_B^u in the direction of B. This lobe encloses fluid which will enter R_0 during the ensuing modulation period. The other shaded lobe in figure 16(a) is the detraining turnstile lobe, L_D, which consists of fluid that will leave R_0 during the ensuing period. As explained in §2, only fluid contained in these two lobes can enter or leave R_0 during this period. As anticipated, L_D overlaps most of L_E, meaning that most of the fluid which enters R_0 leaves again during the same modulation period. This is a consequence of the large amplitude of the modulation relative to the area of R_0 and the long period of the modulation relative to the characteristic orbital period of the fluid recirculating within R_0.

The other sections of W_C^s in figure 16(a) which do not bound the turnstile lobes form pre-images of L_D, i.e. they define lobes containing fluid which will occupy the shaded detraining lobe at some future iteration of the modulation. There are in fact three pre-images of L_D present in figure 16(a), but only parts of two of them can be distinguished: the segment of W_C^s indicated by the asterisk forms part of the first
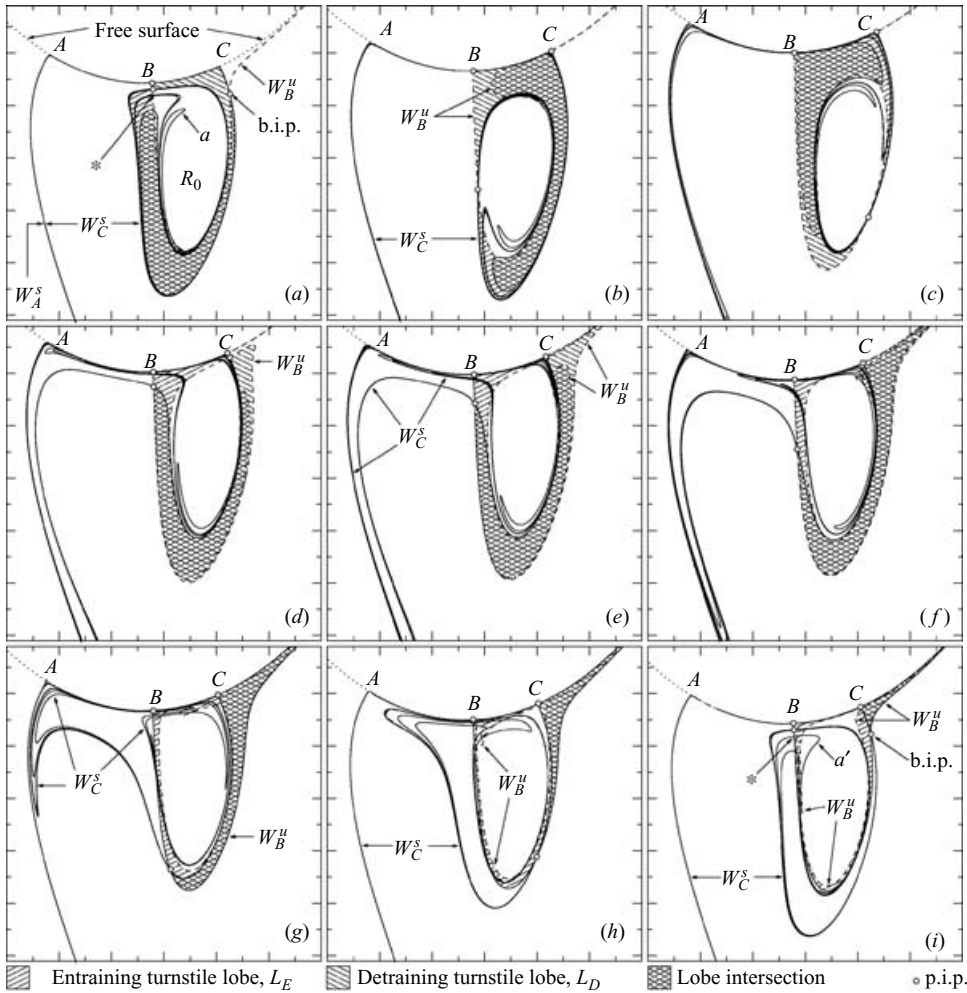
FIGURE 16. A sequence showing the evolution of the stable and unstable manifolds which define the free-surface eddy region. Here $\bar{S} = 1.5$ and $\theta = 20°$. The phase is zero in plots (*a*) and (*i*).

pre-image of L_D, and the segment labelled *a* contains fluid which will form part of the detraining lobe two periods later (after one period *a* maps to *a'* – see figure 16*i*). The remaining parts of these lobes, and the third pre-image, are all compressed against the stable manifold of point *A*, which divides fluid between the left- and right-hand rolls. Note that here the unstable manifold is shown as a dashed line and the stable one as a solid line (this is opposite to the usual convention; otherwise the graphical package inappropriately renders the contorted dashed line as solid). The same effect is seen with W_B^u in the later plots in figure 16 but the manifolds remain distinguishable.

   To assist in visualizing the structure of the manifolds, a schematic is provided in figure 17, where W_B^u is shown as in figure 16(*a*) and W_C^s is shown as in figure 16(*i*). The schematic illustrates how the pre-image of L_D winds through the turnstile, further overlapping L_E. This can also be seen in figure 16(*a*), since part of L_E is enclosed by the segment of W_C^s labelled ∗. This provides a direct illustration of the above discussion regarding the results of Rom-Kedar & Poje (1999) and the rate of tracer
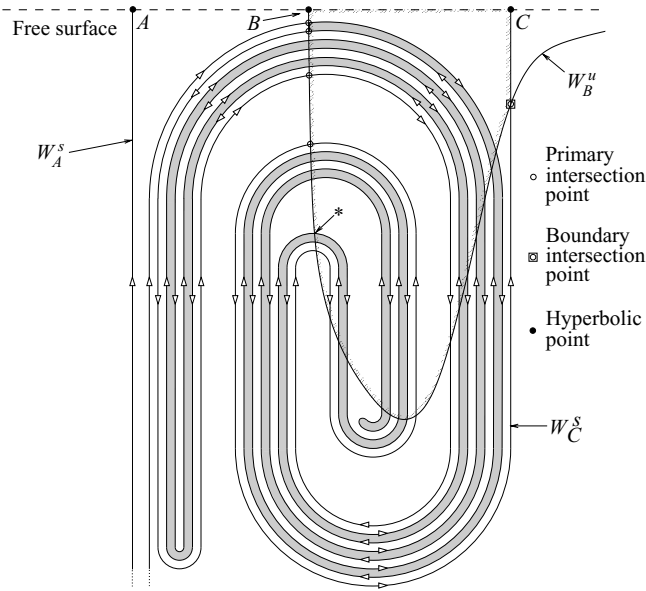
FIGURE 17. A schematic of the manifold structure corresponding to figure $16(a, i)$ illustrating the tortuous way in which the pre-image of the detraining turnstile lobe winds through the turnstile. The secondary intersection point marked by an asterisk corresponds to that in figures $16(a)$ and $16(i)$.

loss from the eddy region: most fluid entrained into R_0 is ejected again either within the same period or the following period.

The sequence in figure 16 shows how the lobes evolve over the period. The evolution is rather different from the fixed-cavity flow of Horner *et al.* (2002), since the free surface is a stress-free boundary which allows fluid motion along it. Therefore as the free surface moves outwards, the entraining lobe moves inwards and appears to 'fill up' all the available space adjacent to the free surface and the segment of W_B^u leaving B. However, manifolds cannot self-intersect or intersect other manifolds of the same stability (see Horner *et al.* 2002), so L_E can only approach and not merge with these curves. As the free surface reaches its maximum extent (figure $16d$), the pre-image of L_E becomes visible, while L_D starts to bulge out in the direction of the right-hand film. This bulge grows as the free surface moves inwards, and the fluid contained in L_D is carried away and out of the domain. At the end of the period (figure $16i$) the parts of L_E which did not overlap L_D lie within R_0, but much of these entrained parts lie within the new detraining lobe (as indeed they always have, due to the invariance of manifold intersections) and so this fluid will be detrained during the following period. Note that the absence of segment a of W_C^s in figure $16(i)$ is merely because too short a length of the manifold has been plotted.

Revisiting figures 9–12 in the light of figure 16 shows how the invariant manifolds fully describe the mechanism of fluid exchange between the eddy and the surrounding fluid in terms of the self-intersecting turnstile construction. Calculating the areas of the turnstile lobes, and accounting for the overlap (Wiggins 1992), gives a measure of the fluid transport rate (Rom-Kedar *et al.* 1990) produced by the modulation. This approach is not particularly practical, however, if one wants to observe say the rate of tracer loss from an eddy over several periods. To do this one would need to account for all the intersections of the turnstile lobes with their images covering the period
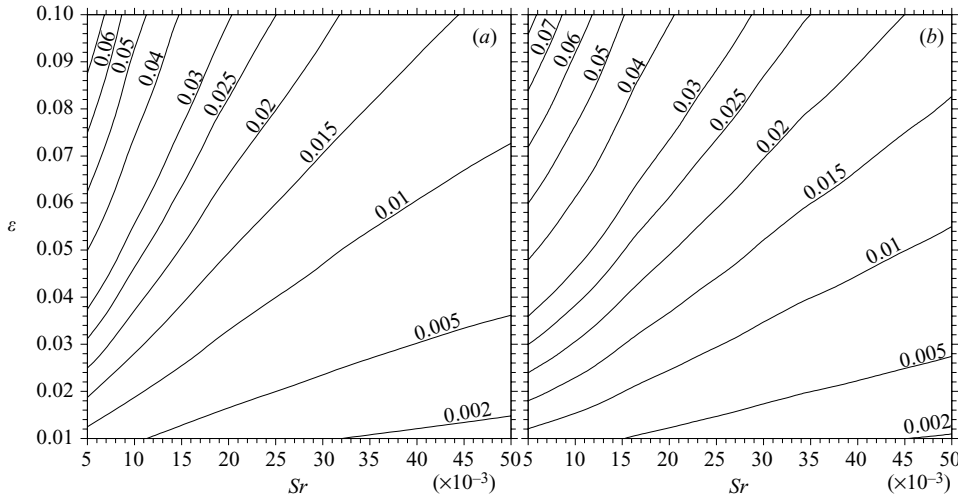
FIGURE 18. Magnitude of the free-surface response as a function of Strouhal number and modulation amplitude: (a) $\bar{S} = 1$; (b) $\bar{S} = 1.5$. The curves are contours of equal δ, with values indicated on the plot.

of interest. Rather than do this, Horner *et al.* (2002) used the unstable manifold to calculate an area coverage, i.e. a percentage of their cavity's area which was occupied by lobes. This approach was also adopted experimentally using dye injection and digital imaging.

A similar approach could be adopted here, as extended calculations of either W_B^u or W_C^s would trace out the boundaries of the unmixed cores in the domain. However, calculations of manifolds are computationally expensive as many tracer points are needed to provide an accurate representation, especially when the manifolds are so highly stretched, curved and folded. The attritional approach adopted above, involving the depletion of tracers from an initially seeded region, is a much cheaper means of obtaining the same result, since the number of 'live' tracers diminishes rather than grows.

5.4. *Frequency effects*

In all the above the frequency of the modulation is constant for each value of $\bar{S}$, since the period of (3.1) is tied to the rotational speeds of the motors. From a computational point of view, it is very easy to replace (3.1) with a purely sinusoidal modulation,

$$S(t) = \bar{S} + \varepsilon \sin 2\pi t, \tag{5.1}$$

where the dimensional frequency, ω, corresponding to the modulation in (5.1) can be changed independently by varying the Strouhal number, $Sr = \omega\sqrt{RH_0}/2\pi U_C$. Recall that time is scaled by the period of the modulation, $T = 2\pi/\omega = L/U_C Sr$. Since there is a lag between a change in roll speed and the response of the free surface, the frequency has a large (and nonlinear) effect on the amplitude, δ, of the free-surface movement. To give an idea of this influence, figure 18 shows contours of equal δ in amplitude–frequency (i.e. ε–Sr) space. As is to be expected, δ increases with increasing ε and decreasing Sr. In the limit $Sr \to 0$, δ tends to the difference in meniscus position between steady states corresponding to $S = \bar{S} \pm \varepsilon$, and $\delta \to 0$ as $Sr \to \infty$. Note that in this plot and all the remaining results, the Reynolds number and other dimensionless parameters (except Sr) are as given in table 1.
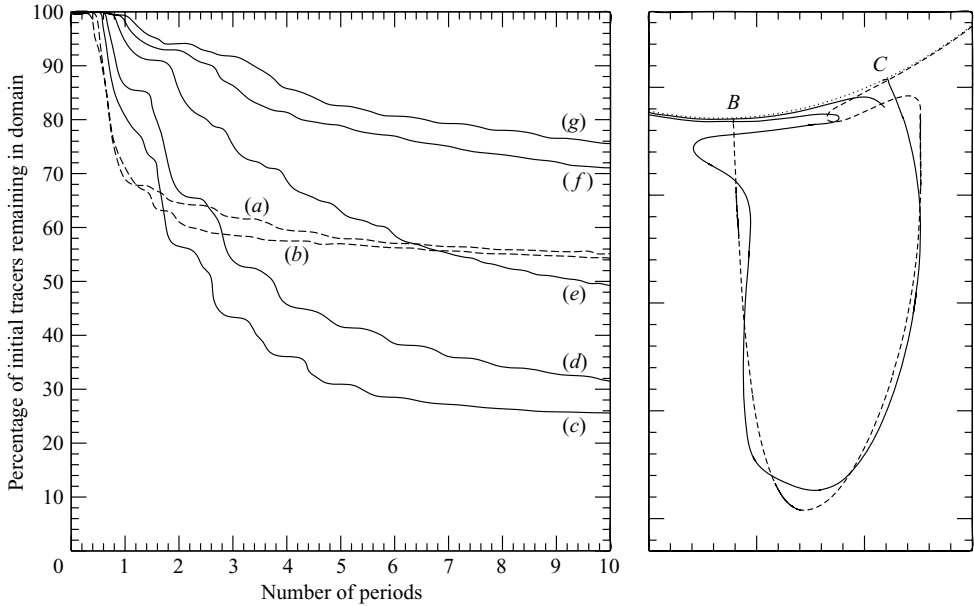
FIGURE 19. Effect of modulation frequency on the rate of tracer loss from the domain: (*a*) $Sr = 0.005$; (*b*) $Sr = 0.01$; (*c*) $Sr = 0.015$; (*d*) $Sr = 0.02$; (*e*) $Sr = 0.03$; (*f*) $Sr = 0.04$; (*g*) $Sr = 0.05$. Other parameters: $\bar{S} = 1.5$, $\varepsilon = 0.1$. Curves (*a*) and (*b*) are shown dashed simply for clarity, to distinguish them from the solid curves that they cross. The right-hand graph shows the unstable (dashed) and stable (solid) manifolds associated with points B and C (see figure 2) for case (*g*). Note that the graphical package renders some sections of the dashed curve as solid.

Taking a particular value of ε, the decrease in δ with Sr suggests that the sizes of the unmixed cores in the domain should increase with Sr. However, Rom-Kedar & Poje (1999) showed that for a periodic Hamiltonian system with a hyperbolic orbit whose manifolds tangle, there exists a universal 'flux function' describing the frequency dependence of the flux through the turnstile. The flux is defined as the area of the entraining turnstile lobe divided by the period of the modulation (here the self-intersection of the turnstile would have to be accounted for, Rom-Kedar & Wiggins 1990). The flux function has the form of a linear increase for small frequency and an exponential decay for large frequency, and therefore features at least one maximum. Hence for each low frequency there should be a corresponding high frequency which yields the same flux. Rom-Kedar & Poje (1999) argued that the high frequency would ultimately result in a greater overall transport of tracer from a given region because the tracer depletion occurs over a larger number of periods, whereas at the low frequency almost all the transport occurs over the first period, as discussed earlier. This suggests that the size of the unmixed cores will be smaller for larger values of Sr. The theory of Rom-Kedar & Poje (1999) is, however, derived for a system with a constant perturbation amplitude, whereas here the presence of the free surface results in a frequency-dependent amplitude.

To determine which of the above effects is dominant, the tracer depletion simulation was repeated for modulation (5.1) and a range of Sr. The results are presented in figure 19. The tracer depletion curves support the assertion of Rom-Kedar & Poje (1999): the low-frequency curves (*a*) and (*b*) show a dramatic drop in tracer population over the first period, then quickly level out, whilst the high-frequency curves show a
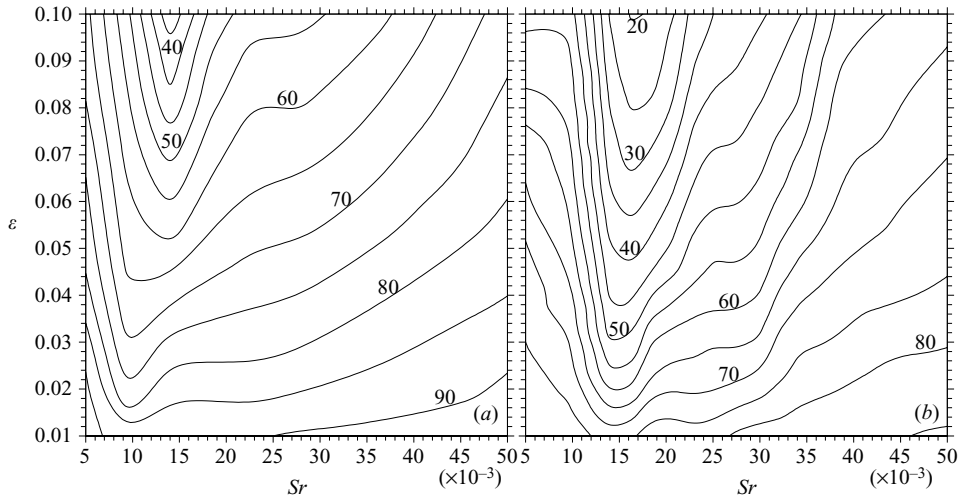
FIGURE 20. Contours in frequency–amplitude space indicating the percentage of initial points remaining inside the domain after 30 periods of sinusoidal modulation: (*a*) $\bar{S} = 1$; (*b*) $\bar{S} = 1.5$. The contour interval is 5 %.

more gradual depletion which continues over a greater number of periods. Thus there is an optimum frequency which produces the most effective stirring, i.e. the smallest unmixed cores.

By way of contrast to the earlier manifold plots (figure 16), the right-hand graph in figure 19 shows the manifolds for the case $\bar{S} = 1.5$, $\varepsilon = 0.1$ and $Sr = 0.05$ (i.e. corresponding to the curve *g* in figure 19). In this case the free-surface movement is much smaller, resulting in thinner lobes, and the period of the modulation is much shorter. Hence the lobes are also shorter, and fluid which is entrained is not able to travel completely round the recirculation and exit again within the same modulation cycle. Therefore the turnstile lobes do not intersect, and the structure matches that in the schematic of figure 3(*a*).

Balasuriya (2005) has recently considered the optimization problem of determining the form of modulation (subject to an upper bound) which delivers the maximum flux for a given frequency in dynamical systems undergoing time-harmonic perturbations. The analysis is based on the manipulation of invariant manifolds to maximize lobe areas, and exploits the Melnikov function to obtain the signed distance between manifolds. It therefore relies on the form of the perturbation to the Hamiltonian being known explicitly. Similarly, the more specific optimization problem tackled numerically by Noack *et al.* (2004) relies on a direct perturbation of the underlying Hamiltonian system in order for control theory to be applied. In the present work the form of the perturbation to the Hamiltonian is not known. Coupled with the nonlinear dynamics of the free surface, this makes optimization of the perturbation to achieve maximum transport a significant challenge.

While the optimization problem is beyond the scope of this initial study, figure 20 summarizes the influence of frequency and amplitude on transport out of the eddy region for the sinusoidal perturbation considered here. The figure shows contours giving the percentage of initial tracers remaining in the domain after 30 modulation cycles (after which the curves in figure 19 have levelled out much more). The contours show that for each amplitude there is one particular frequency which delivers the
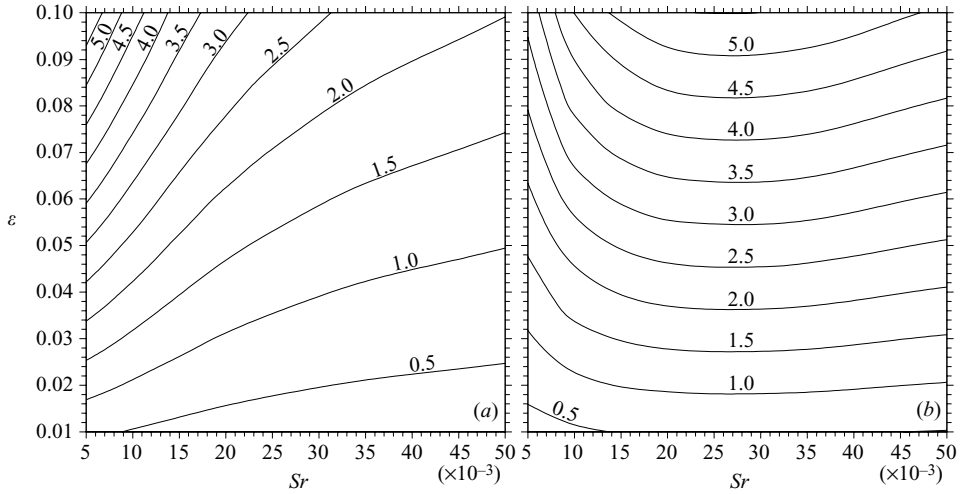
FIGURE 21. Contours showing the percentage change in film thickness as a function of modulation frequency and amplitude for the case $\bar{S} = 1.5$: (*a*) film on constant-speed roll; (*b*) film on modulated roll.

most effective transport, and that this frequency increases with amplitude. At high frequencies the free surface does not 'see' the rapid changes in roll speed, and the amplitude of the perturbation diminishes, with a consequent reduction in the overall transport.

6. Implications for the industrial context

6.1. *Modulation side effects*

Given that the flow investigated here arises in the coating industry, it seems appropriate to address the side effects of the modulations discussed above. The particular concern is the impact upon the outgoing film thicknesses, since most coating applications require films of uniform thickness (recall that in a practical situation a substrate would be wrapped around one of the rolls so that it is continuously coated). The modulations (3.1) and (5.1) will clearly produce a periodic disturbance on the films, with a wavelength of $\ell = 2\pi R\Omega/\omega = cL/Sr$, where Ω is the angular velocity of the roll, ω is the frequency of the modulation, and $c = 1$ or $\bar{S}$ depending on the roll. Figure 21 shows the amplitude of the disturbance as a function of ε and Sr when $\bar{S} = 1.5$, with the (peak–peak) amplitude expressed as a percentage of the mean film thickness for each roll. The two films show quite different responses. The contours for the film on the unmodulated roll are the same shape as those for the meniscus tip movement (figure 18*b*), which is perhaps not surprising given that the variation in this film is almost in phase with the free-surface movement, i.e. the film thins as the free surface moves inwards. On the other hand, the film on the modulated roll (which varies roughly in antiphase to the other film – see figure 6*a, b*) varies more strongly for frequencies in the middle of the range considered. The frequency producing the largest disturbance does not correspond to that giving the greatest transport, however.

The percentage change in film thickness for each film is rather less than the percentage change in roll speed. Whether or not such variations are acceptable will depend on the application; some high-precision coating processes may require a wet film thickness variation below 1 % to ensure a good quality dry film (Schweizer 1997).

Once the films leave the coating bead, capillarity (and gravity, depending on the substrate orientation) will act to help level the films (Kheshgi 1997), but this may require more time than is available before the next stage in the continuous coating process, particularly for long-wavelength perturbations. Orchard (1962) considered the levelling by surface tension of a film of mean thickness $\bar{H}$, whose initial profile was given by a Fourier series, and derived an exponential decay time, $T_L = 3\mu\ell^4/16\pi^4\gamma\bar{H}^3$ (ℓ being the wavelength), valid for thin films with disturbances having a small amplitude-to-wavelength ratio. Considering the film on the modulated roll (with dimensionless mean thickness $\bar{h}_m$), this becomes

$$T_L = \left(\frac{3\bar{S}^4}{16\pi^4\bar{h}_m^3}\right)\left(\frac{\mu L}{\gamma}\right)\left(\frac{1}{Sr}\right)^4, \tag{6.1}$$

and one can see that small values of Sr will result in very long decay times. In fact, for the experimental model rig and high-viscosity oil used here, and the range of Sr in figure 21, T_L is of the order $10^4 - 10^8$ s, indicating that levelling due to surface tension in any practical situation would be insignificant.

In addition to being directly applied to a substrate, the films generated by the roll-pair considered here could instead be passed into the gaps between subsequent rolls forming part of a much larger coating machine. In this case one would have to explore the effects of a varying input flux in the subsequent gap to assess how the disturbance is propagated through or perhaps diminished by further stages of the process. In any case, it is clear that due consideration must be given to effects of any modulation before it can be used for practical purposes.

6.2. 'Counter-modulation'

For a given modulation frequency, the thicknesses of the two films leaving the domain are primarily influenced by the relative speeds of the rolls (i.e. $S = u_m/u_c$) and the flux of fluid entering the domain through the nip (i.e. λ). However, λ is essentially proportional to the average of the peripheral speeds of the two rolls,

$$\lambda \propto \bar{u} = \tfrac{1}{2}(u_m + u_c), \tag{6.2}$$

and so one might ask if it is possible to introduce a second speed modulation, on roll C, such that the variation in one or both films is reduced.

As far as the flux is concerned, it is evident from (6.2) that a second modulation of equal amplitude but opposite phase would counter the first modulation, giving a practically constant λ. Unfortunately this would also act to increase S, and would therefore be unlikely to reduce the film thickness variations. Finding the correct phase and amplitude of the second modulation is clearly not a trivial task, but a reasonably effective counter-modulation can be found by replacing the single modulation (5.1) with a modulation of amplitude $\tfrac{1}{2}\varepsilon$ on each roll, i.e.

$$u_m = \bar{S} + \tfrac{1}{2}\varepsilon\sin 2\pi t, \tag{6.3}$$

$$u_c = 1 + \tfrac{1}{2}\varepsilon\sin 2\pi(t + \phi_c), \tag{6.4}$$

where ϕ_c is a phase difference between the two modulations. The effect of this dual modulation on the film thickness variations and the size of the unmixed cores is shown in table 2, where $\bar{S} = 1.5$, $\varepsilon = 0.1$, and $Sr = 0.015$.

The table shows that spreading the flow modulation over both rolls produces a dramatic reduction in the variation of the film thickness on roll M, without a correspondingly large increase in the size of the unmixed regions. By introducing a

ϕ_c	Roll M	Roll C	N_{30}
0.0	1.9 %	3.5 %	31.2 %
0.1	1.2 %	4.7 %	26.8 %
0.2	1.5 %	5.7 %	22.7 %
0.3	2.3 %	6.2 %	20.7 %
0.4	3.1 %	6.3 %	20.5 %
0.5	3.6 %	6.0 %	22.5 %
—	(5.1 %)	(3.9 %)	(23.3 %)

TABLE 2. Effect of modulation phase difference, ϕ_c, on film thickness variations and unmixed core size when both roll speeds are modulated sinusoidally with amplitude 0.05 and $Sr = 0.015$ ($\bar{S} = 1.5$). The second and third columns give the amplitudes of the film thickness variations expressed as a percentage of the mean film thickness on each roll. The fourth column, N_{30}, shows the percentage of tracers remaining in the domain after 30 modulation cycles starting from an initial state where the recirculation region was uniformly seeded with tracers. For comparison, the last line in the table gives the corresponding values for the case of a single speed modulation of amplitude 0.1.

small phase difference between the two rolls, the variation in film thickness on roll M can be reduced further, to just 1.2 %, but at the expense of a larger variation in the other film thickness. The phase difference also improves the transport characteristics of the dual modulation by reducing the size of the unmixed regions which remain in the domain. This simple example demonstrates that, by careful choice of modulations, effective stirring should be possible without excessive perturbation of at least one of the films.

7. Conclusion

The effect of a periodic flow modulation on fluid transport from a recirculation region bounded by a free surface has been explored using a numerical method validated against experiments. The flow was modulated by continuously varying the speed of one of the driving rolls, and in the experiments this was achieved using a Hooke's joint. When the drive speed is varied, the free surface changes shape and position, and this non-tangential motion drives fluid exchange between the recirculation region and the surrounding flow. The amplitude of the free-surface motion is strongly dependent on the frequency of the modulation. At high frequencies the free surface is unable to respond quickly enough for the changes in roll speed to affect its position, and its motion is therefore limited. For small frequencies a much larger response is seen, but the dynamics of the free surface mean that a quasi-steady approach is not possible even for small frequencies. A full time-dependent simulation is required.

Focusing on the eddy which is attached to the free surface, experimental and numerical flow visualizations show that fluid is drawn into the eddy region along the free surface as the surface moves outwards, thus increasing the volume of the eddy. When the free surface returns, fluid is ejected along the free surface into the film on the modulated roll. Calculations of the stable and unstable manifolds associated with periodic points on the free surface reveal that for small frequencies fluid exchange is governed by a self-intersecting turnstile mechanism, such that much of the fluid entrained in a given modulation cycle is ejected during the same cycle. This is a consequence of the relatively large perturbation compared to the size of the eddy,

and the relatively high orbital frequency of fluid in the eddy, which allows entrained fluid to travel completely round the eddy within half a modulation period. Higher modulation frequencies do not permit the latter effect, even for large modulation amplitudes, and for these cases the turnstile lobes do not intersect. Despite introducing many complicating factors into the simulation of the flow, the free surface itself does not play a part in the lobe dynamics, since the manifolds which lie along it cannot tangle because the free surface is a material interface.

While manifolds provide a very clear picture of the fluid transport mechanism over one period, they are impractical for the study of transport over several periods. Instead, this behaviour is studied by observing the depletion of tracer particles initially distributed uniformly throughout the region of interest. Results show a consistency with the theoretical results of Rom-Kedar & Poje (1999) in that for small frequencies most transport is complete after one modulation cycle, whereas for high frequencies detrainment of tracers occurs at a more gradual rate but over a longer time scale. By considering the percentage of tracers left after 30 modulation periods, contours in frequency–amplitude space could be constructed, and these show that for each amplitude there is a particular frequency which delivers the most effective transport. This frequency increases slightly with amplitude. For high frequencies, the corresponding decrease in the amplitude of the free-surface motion results in poor transport.

The periodic modulation of the free-surface flow has been shown to offer enhanced transport of fluid into and out of regions in which fluid is trapped in the unperturbed state. However, a possible drawback of this approach from an industrial point of view is the side effect on the liquid films produced by the flow. The modulation generates a variation in film thickness, with the percentage change in thickness approximately one quarter of the percentage change in roll speed. This variation in film thickness can be substantially reduced, however, by introducing a carefully chosen second modulation on the previously unmodulated roll. Though this work has focused on a roll coating configuration, the methods described could equally well be applied to other geometries and other types of modulation, for example a pulsed flow rate.

REFERENCES

ANDERSON, P. D., GALAKTIONOV, O. S., PETERS, G. W. M., VAN DE VOSSE, F. N. & MEIJER, H. E. H. 2000*a* Mixing of non-Newtonian fluids in time-periodic cavity flows. *J. Non-Newtonian Fluid Mech.* **93**, 265–286.

ANDERSON, P. D., GALAKTIONOV, O. S., PETERS, G. W. M., VAN DE VOSSE, F. N. & MEIJER, H. E. H. 2000*b* Chaotic fluid mixing in non-quasi-static time-periodic cavity flows. *Intl J. Heat Fluid Flow* **21**, 176–185.

AREF, H. 1984 Stirring by chaotic advection. *J. Fluid Mech.* **143**, 1–21.

BALASURIYA, S. 2005 Optimal perturbation for enhanced chaotic transport. *Physica* D **202**, 155–176.

BEIGIE, D., LEONARD, A. & WIGGINS, S. 1994 Invariant manifold templates for chaotic advection. *Chaos Soliton. Fract.* **4**(6), 749–868.

CHIEN, W.-L., RISING, H. & OTTINO, J. M. 1986 Laminar mixing and chaotic mixing in several cavity flows. *J. Fluid Mech.* **170**, 355–377.

COYLE, D. J., MACOSKO, C. W. & SCRIVEN, L. E. 1986 Film-splitting flows in forward roll coating. *J. Fluid Mech.* **171**, 183–207.

COYLE, D. J., MACOSKO, C. W. & SCRIVEN, L. E. 1990 Stability of symmetric film-splitting between counter-rotating cylinders. *J. Fluid Mech.* **216**, 437–458.

FINN, M. D. & COX, S. M. 2001 Stokes flow in a mixer with changing geometry. *J. Engng Maths* **41**, 75–99.

GALAKTIONOV, O. S., ANDERSON, P. D. & PETERS, G. W. M. 2002 Structure development during chaotic mixing in the journal bearing flow. *Phys. Fluids* **14**, 3009–3017.

GASKELL, P. H., INNES, G. E. & SAVAGE, M. D. 1998*a* An experimental investigation of meniscus roll coating. *J. Fluid Mech.* **355**, 14–44.

GASKELL, P. H., KAPUR, N. & SAVAGE, M. D. 2001 Bead-break instability. *Phys. Fluids* **13**, 1243–1253.

GASKELL, P. H., SAVAGE, M. D., SUMMERS, J. L. & THOMPSON, H. M. 1995 Modelling and analysis of meniscus roll coating. *J. Fluid Mech.* **298**, 113–137.

GASKELL, P. H., SAVAGE, M. D. & THOMPSON, H. M. 1998*b* Stagnation-saddle points and flow patterns in Stokes flow between contra-rotating cylinders. *J. Fluid Mech.* **370**, 221–247.

GASKELL, P. H., THOMPSON, H. M., SAVAGE, M. D. & IKIN, J. B. 1999 Steady recirculating flow near static contact lines. *Chem. Engng Sci.* **54**, 819–828.

GUTOFF, E. B. 1993 Avoid coating and drying defects. *Chem. Engng Prog.* **89**, 49–55.

HALL, A. S., HOLOWENKO, A. R. & LAUGHLIN, H. G. 1961 *Theory and Problems of Machine Design.* Schaum Publishing Co., New York.

HORNER, M., METCALFE, G., WIGGINS, S. & OTTINO, J. M. 2002 Transport enhancement mechanisms in open cavities. *J. Fluid Mech.* **452**, 199–229.

JANA, S. C., TJAHJADI, M. & OTTINO, J. M. 1994 Chaotic mixing of viscous fluids by periodic changes in geometry: baffled cavity flow. *AIChE J.* **40**, 1769–1781.

JIMACK, P. K. & WATHEN, A. J. 1991 Temporal derivatives in the finite-element method on continuously deforming grids. *SIAM J. Numer. Anal.* **28**, 990–1003.

KAPER, T. J. & WIGGINS, S. 1993 An analytical study of transport in Stokes flows exhibiting large-scale chaos in the eccentric journal bearing. *J. Fluid Mech.* **253**, 211–243.

KHESHGI, H. S. 1997 The fate of thin liquid films after coating. In *Liquid Film Coating* (ed. S. F. Kistler & P. M. Schweizer). Chapman & Hall, London.

KISTLER, S. F. & SCRIVEN, L. E. 1983 Coating flows. In *Computational analysis of polymer processing* (ed. J. R. A. Pearson & S. M. Richardson). Applied Science, London.

KUMAR, S. & HOMSY, G. M. 1996 Chaotic advection in creeping flow of viscoelastic fluids between slowly modulated eccentric cylinders. *Phys. Fluids* **8**, 1774–1787.

MALHOTRA, N. & WIGGINS, S. 1998 Geometric structures, lobe dynamics, and Lagrangian transport in flows with aperiodic time-dependence, with applications to Rossby wave flow. *J. Nonlinear Sci.* **8**, 401–456.

MANCHO, A. M., SMALL, D. & WIGGINS, S. 2006 A comparison of methods for interpolating chaotic flows from discrete velocity data. *Comput. Fluids* **35**, 416–428.

MATHEWS, J. H. 1992 *Numerical Methods for Mathematics, Science and Engineering*, 2nd edn. Prentice-Hall.

NISHIMURA, T. & KUNITSUGU, K. 1997 Fluid mixing and mass transfer in two-dimensional cavities with time-periodic lid velocity. *Intl J. Heat Fluid Flow* **18**(5), 497–506.

NOACK, B. R., MEZIĆ, I., TADMOR, G. & BANASZUK, A. 2004 Optimal mixing in recirculation zones. *Phys. Fluids* **16**, 867–888.

NOAKES, C. J., GASKELL, P. H., THOMPSON, H. M. & IKIN, J. B. 2002 Streak-line defect minimization in multi-layer slide coating. *Trans. IChemE* **80**, A, 449–463.

ORCHARD, S. E. 1962 On surface levelling in viscous liquids and gels. *Appl. Sci. Res.* A **11**, 451–464.

OTTINO, J. M. 1989 *The Kinematics of Mixing: Stretching, Chaos and Transport*. Cambridge University Press.

PAPANASTASIOU, T. C., MALAMATARIS, N. & ELLWOOD, K. 1992 A new outflow boundary condition. *Intl J. Numer. Meth. Fluids* **14**, 587–608.

PITTS, E. & GREILLER, J. 1961 The flow of thin liquid films between rollers. *J. Fluid Mech.* **11**, 33–50.

ROM-KEDAR, V., LEONARD, A. & WIGGINS, S. 1990 An analytical study of transport, mixing and chaos in an unsteady vortical flow. *J. Fluid Mech.* **214**, 347–394.

ROM-KEDAR, V. & POJE, A. C. 1999 Universal properties of chaotic transport in the presence of diffusion. *Phys. Fluids* **11**, 2044–2057.

ROM-KEDAR, V. & WIGGINS, S. 1990 Transport in two-dimensional maps. *Arch. Rat. Mech. Anal.* **109**(3), 239–298.

ROSENFELD, M. 1995 Utilization of Fourier decomposition for analyzing time-periodic flows. *Comput. Fluids* **24**(4), 349–368.

ROSENFELD, M. 1996 Calculation of streaklines for time periodic flows. *AIAA J.* **34**, 79–82.

SCHWEIZER, P. M. 1997 Experimental methods. In *Liquid Film Coating* (ed. S. F. Kistler & P. M. Schweizer). Chapman & Hall, London.

SOUVALIOTIS, A., JANA, S. C. & OTTINO, J. M. 1995 Potentialities and limitations of mixing simulations. *AIChE J.* **41**, 1605–1621.

SUMMERS, J. L. 1995 Variable-coefficient harmonic balance for periodically forced nonlinear operators. *Nonlinear Dyn.* **7**, 11–35.

SUMMERS, J. L., THOMPSON, H. M. & GASKELL, P. H. 2004 Flow structure and transfer jets in a contra-rotating rigid-roll coating system. *Theor. Comput. Fluid Dyn.* **17**(3), 189–212.

SWANSON, P. D. & OTTINO, J. M. 1990 A comparative computational and experimental study of chaotic mixing of viscous fluids. *J. Fluid Mech.* **213**, 227–249.

TJAHJADI, M. & FOSTER R. W. 1996 Single screw extruder capable of generating chaotic mixing. US Patent No. 5 551 777.

WICKS, P. J., DECRÉ, M., PLANQUART, PH. & BUCHLIN, J. M. 1995 Flow topology associated with disjoint eddies in an asymmetric film-splitting problem. *Phys. Rev.* E **52**(2), R1281–R1284.

WIERSCHEM, A. & AKSEL, N. 2004 Influence of inertia on eddies created in films creeping over strongly undulated substrates. *Phys. Fluids* **16**, 4566–4574.

WIGGINS, S. 1992 *Chaotic transport in dynamical systems.* Springer.

YAO, W. G., TAKAHASHI, K., KOYAMA, K. & DAI, G. C. 1997 Design of a new type of pin mixing section for a screw extruder based on analysis of flow and distributive mixing performance. *Chem. Engng Sci.* **52**, 13–21.